Analysis of Swath Bathymetry Sonar Accuracy

John S. Bird, *Member, IEEE,* and Geoff K. Mullins

***Abstract*—The practical limitations of many bottom mapping sonars lie in their ability to accurately estimate the angle of arrival. This paper addresses the accuracy of angle estimation when employed to determine the location of an extended target such as the bottom. A Gaussian model is assumed for the bottom backscatter and the corresponding Cramer–Rao lower bound for the variance of the angle estimate is determined for multi-element linear arrays. The paper focuses on determining the performance of high-resolution swath bathymetry sonars and, therefore, concentrates on the ability to determine bottom location with short pulses. Two error mechanisms, footprint shift and uncorrelated noise, are identified as important contributors to measurement errors. The two-element interferometric sonar configuration is investigated in detail. It is shown through the use of probability distributions, the Cramer–Rao bound, and simulation that it is difficult to get a good estimate of performance through simulation alone. Performance enhancement through pre-estimation and post-estimation averaging of multiple snapshots and changes in performance with pulse length and pulse rise time are also considered. Bottom estimation performance employing multi-element arrays is compared and contrasted with that of the two-element interferometric array. It is determined that there is little benefit associated with the multi-element array in terms of angle estimation performance alone. However, when other considerations such as angle ambiguities, multiple angles of arrival, and physical shortcomings associated with practical arrays are taken into account, the multi-element array is favored.**

***Index Terms*—Bottom estimation, footprint shift, interferometric sonar, swath bathymetry.**

I. Introduction

MANY sonars employed for bottom mapping use some form of angle estimation to determine the location of the bottom. The range to the bottom is known from the time of flight of the acoustic pulse. The direction to the bottom for a particular time is estimated from the backscatter signals received on an array of acoustic elements. The simplest form of these swath bathymetry sonars uses the phase difference between two acoustic elements separated by a small distance to determine the angle of arrival (AOA). These sonars are known as interferometric sonars and the history of their development is recorded in [1], [2], and associated references.

Interferometric sonars, however, do not work well in situations where backscatter is received from multiple angles at the same time, because with two elements, it is possible to estimate only one angle. Multi-angle swath bathymetry (MASB) sonars were developed to work in more complex environments such as shallow water where acoustic multipath signals are expected. These sonars use multiple array elements to resolve multiple angles of arrival [3], [4]. MASB systems have certain advantages when compared to multibeam systems, which include inherent colocation of bathymetry with sidescan imagery and crosstrack resolution determined by pulse length rather that beamwidth, which in turn allows fewer transducer elements and channels to be used. Disadvantages include lower resolution near nadir and less ability to resolve complex target geometries.

In applications suited to the MASB configuration, the issue of angle estimation accuracy arises. Lurton [5] addresses this problem for two-element arrays where he introduces the concept of footprint shift as a mechanism of angle estimation errors. In this paper, we extend the analysis to include multiple-element arrays and multiple snapshots of the array signals and thereby address the performance of MASB systems. The performance of the two-element interferometric sonar configuration is also covered in detail because previous results did not include specific details about the difficulty of evaluating angle estimation performance. Also included in the analysis is the performance associated with a practical pulse shape that includes not only the effect of pulse length but also pulse rise times. It is shown through simulation and analysis that the Cramer–Rao bound is a valuable tool for predicting the performance of interferometric and MASB sonar systems. The analysis also shows that for practical pulse shapes, there is little difference in terms of angle estimation accuracy between a multiple-element array and a two-element array with a spacing equal to the outside spacing of the multiple-element array. However, other issues are outlined that heavily favor the use of a multiple-element array.

The analysis begins in Section II wherein the Cramer–Rao lower bound (CRLB) for estimating the AOA of bottom backscatter with a multiple-element array is developed, assuming that the backscatter can be modeled as a circular symmetric Gaussian signal. This assumption was made for the signal model for four reasons. First, there is evidence that some backscatter is of this type in [6]. Second, other authors [5] have used this model, and therefore, results can be compared. Third, the analysis is possible with this model, and it is not as yet with other models. Finally, the model allows us to develop trends so that even if it does not hold in a specific case, the trends uncovered might. In Section III, the two-element interferometric sonar is analyzed in detail with regard to its ability to estimate the AOA. The probability density of the angle is presented along with analysis and simulations that show that the true variance of the angle estimate is very difficult to obtain through simulation. Hence, simulation without supporting analysis is not sufficient to evaluate performance. Furthermore, in Section III, an analysis of the two-element array is extended

Manuscript received March 17, 2004; revised February 28, 2005; accepted March 9, 2005. The authors acknowledge the support of the Natural Science and Engineering Research Council in Canada, the Advanced Systems Institute of B.C., and International Submarine Engineering Ltd. Associate Editor: D. J. Tang.

The authors are with the Engineering Science Department, Simon Fraser University, Burnaby, BC V5A 1S6, Canada (e-mail: jbird@sfu.ca; gkm@sfu.ca).

Digital Object Identifier 10.1109/JOE.2005.850869

to include multiple snapshots and two methods of processing the snapshots: pre-estimation averaging and post-estimation averaging. It is shown that pre-estimation averaging outperforms post-estimation averaging for the model given, but that post-estimation averaging is more robust to domination by a few strong scatterers.

In Section IV, the performance gain of multiple-element arrays is given with respect to the effects of both footprint shift and uncorrelated noise. It is shown that because of the decorrelation effect of footprint shift, the gain achieved over this mechanism for errors is not as great as the gain achieved over uncorrelated noise.

Section V contains a general discussion and conclusions. The performance of three arrays is compared and contrasted. The arrays consist of a two-element array with spacing $\lambda/2$ (where λ is the wavelength), a six-element array with element spacing $\lambda/2$, and another two-element array with spacing equal to the spacing of the outside elements of the six-element array, namely $5(\lambda/2)$. It is determined that for practical pulse shapes, the three arrays are relatively similar in performance against the footprint shift effect, while the latter two arrays perform better against uncorrelated noise for estimating the AOA and, hence, the bottom location.

The general conclusion of the paper is that multiple-element arrays and two-element arrays with the same outside spacing perform similarly in terms of angle estimation, but the multiple-element array is preferred when multiple angles of arrival, angle ambiguities, and array imperfections are issues, as is usually the case.

II. Development of the Cramer–Rao Lower Bound

In this section, the CRLB for estimating the AOA of bottom returns from a linear array of M elements is determined. The development includes some ideas found in [5] and [6]. The resulting model is that of a complex Gaussian signal in complex Gaussian noise for which the CRLB can be determined from the covariance matrix as follows [7]:

$$J_{ik} = N \operatorname{trace}\left\{\mathbf{R}^{-1}\frac{\partial \mathbf{R}}{\partial u_i}\mathbf{R}^{-1}\frac{\partial \mathbf{R}}{\partial u_k}\right\} \tag{1}$$

where J_{ik} is the (i,k)th entry in the Fisher information matrix, each u_p is a parameter to be estimated, $\mathbf{R}$ is the covariance matrix, and N is the number of independent snapshots taken with the array.

For the problem at hand, it is assumed that the only unknown parameter is the AOA, and therefore, the Fisher information matrix is a scalar. Hence, the CRLB for the variance of any unbiased estimator of the arrival angle is

$$\text{CRLB}(\gamma) = \frac{1}{J}. \tag{2}$$

In (2), γ is the electrical arrival angle (i.e., the phase difference from array element to array element) from which the physical arrival angle θ is determined through the relation

$$\gamma = \frac{2\pi d}{\lambda}\sin(\theta) \tag{3}$$

where λ is the wavelength and d is the spacing between array elements. The CRLB for the physical angle θ can be determined from the CRLB for γ through a simple transformation [7, p. 929].

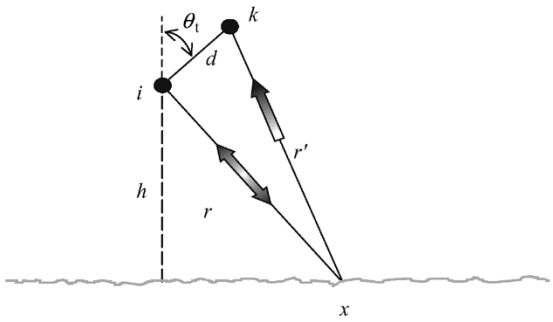

Fig. 1. Geometry for determining distance to acoustic array elements.

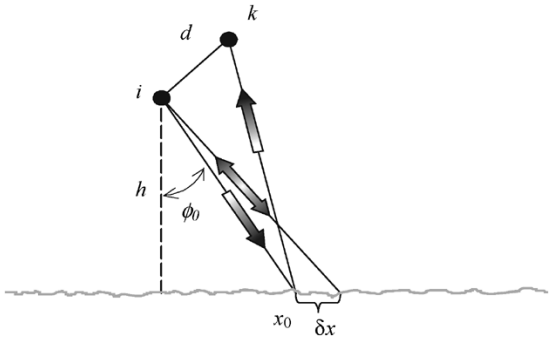

Fig. 2. Geometry for determining the footprint shift.

The first step in obtaining the bound is to derive the form of the correlation matrix $\mathbf{R}$. For an array of receive elements, the correlation matrix is defined as

$$\mathbf{R} = \mathrm{E}\{ss^{\mathrm{H}}\} = \begin{pmatrix} \mathrm{E}\{s_1 s_1^*\} & \cdots & \mathrm{E}\{s_1 s_m^*\} \\ \vdots & \ddots & \vdots \\ \mathrm{E}\{s_m s_1^*\} & \cdots & \mathrm{E}\{s_m s_m^*\} \end{pmatrix} \tag{4}$$

where $s = [\,s_1 \quad s_2 \quad \cdots \quad s_m\,]^{\mathrm{T}}$ and s_i is the narrowband complex signal received at element i. Therefore, to determine $\mathbf{R}$ for the bottom estimation problem, $\mathrm{E}\{s_k s_i^*\}$ must be found for arbitrary array elements i and k.

Assuming that the signal from a particular set of bottom scatters is received at elements i and k, the following relations hold:

$$\begin{aligned} s_i &= \int s_i(x) b(x) \mathrm{e}^{j\frac{4\pi r(x)}{\lambda}} dx \\ s_k &= \int s_k(x) b(x) \mathrm{e}^{j\frac{4\pi (r(x)+r'(x))}{2\lambda}} dx \end{aligned} \tag{5}$$

where the integrals are delimited by the signal pulse, $b(x)$ is the scattering function of the bottom scatterers, which is assumed to be complex Gaussian with $\mathrm{E}\{b(x)b(y)^*\} = \delta(x-y)E\{|b|^2\}$, and $r(x)$ and $r'(x)$ are defined in Fig. 1.

With the help of Fig. 2, the following expressions for $s_i(x)$ and $s_k(x)$ are obtained consistent with the bottom shift model of [5]

$$\begin{aligned} s_i(x) &= \sqrt{E_t}\, s(x_0 + \delta x - x) \\ s_k(x) &= \sqrt{E_t}\, s(x_0 - x) \end{aligned} \tag{6}$$

where $\sqrt{E_t}$ is the signal amplitude and $s()$ is the pulse shape on the bottom. It is assumed that the pulse is normalized so that $\int s(x)^2 dx = 1$. In other words, $s_i(x)$ is made up of scatters over

the range $[x_0+\delta x-\Delta x, x_0+\delta x]$, where Δx is the pulse length on the bottom. $s_k(x)$ is made up of scatterers over the range $[x_0-\Delta x, x_0]$. For each s_i and s_k, the integral sums over these ranges of x. The variable δx represents the shift on the bottom resulting from element k receiving signals from a slightly different part of the bottom than element i. For this geometry, δx is derived in Appendix I and is well approximated by

$$\delta x = \frac{d}{2}\frac{\cos(\phi_0+\theta_t)}{\sin(\phi_0)} = \frac{d}{2}\frac{\sin(\theta)}{\sin(\phi_0)} \tag{7}$$

where d is the element separation, ϕ_0 is defined in Fig. 2, and θ_t is the tilt of the array from the horizontal, and θ is the physical AOA relative broadside the array.

The pulse length on the bottom represented by Δx is

$$\Delta x = \frac{cT}{2\sin(\phi_0)}. \tag{8}$$

With these definitions, the signals received on the two elements i and k at the same time are

$$\begin{aligned} s_i &= \sqrt{E_t}\int s(x_0+\delta x-x)b(x)\mathrm{e}^{j\frac{4\pi r(x)}{\lambda}}dx \\ s_k &= \sqrt{E_t}\int s(x_0-x)b(x)\mathrm{e}^{j\frac{4\pi\left(r(x)+r'(x)\right)}{2\lambda}}dx. \end{aligned} \tag{9}$$

Utilizing the form of the correlation function for $b(x)$, the corresponding correlation of s_i and s_k is given by

$$\begin{aligned} \mathrm{E}\left\{s_k s_i^*\right\} &= E_t\mathrm{E}\left\{|b|^2\right\} \\ &\times\int s(x_0+\delta x-x)^* s(x_0-x)\mathrm{e}^{j\frac{2\pi}{\lambda}\left(r'(x)-r(x)\right)}dx. \end{aligned} \tag{10}$$

From the geometry in Fig. 1

$$\begin{aligned} r'(x)-r(x) &= r(x)\sqrt{1+\frac{2d_{ik}}{r(x)}\cos\left(\phi(x)+\theta_t\right)} \\ &\simeq d_{ik}\cos\left(\phi(x)+\theta_t\right). \end{aligned} \tag{11}$$

So that

$$\begin{aligned} \mathrm{E}\left\{s_k s_i^*\right\} &= E_t\mathrm{E}\left\{|b|^2\right\} \\ &\times\int s(x_0+\delta x-x)^* s(x_0-x)\mathrm{e}^{j\frac{2\pi}{\lambda}d_{ik}\cos\left(\phi(x)+\theta_t\right)}dx. \end{aligned} \tag{12}$$

Following [6] and expanding $\cos(\phi(x)+\theta_t)$ around ϕ_0 as defined in Fig. 2 and retaining the first two terms

$$\begin{aligned} \cos\left(\phi(x)+\theta_t\right) &\simeq \cos\left(\phi_0+\theta_t\right) \\ &-\frac{\sin(\phi_0+\theta_t)\cos^2(\phi_0)}{h}(x-x_0) \end{aligned} \tag{13}$$

and substituting (13) into (12) results in

$$\begin{aligned} \mathrm{E}\left\{s_k s_i^*\right\} &= E_t\mathrm{E}\left\{|b|^2\right\}\mathrm{e}^{j\frac{2\pi d_{ik}}{\lambda}\cos\left(\phi_0+\theta_t\right)} \\ &\times\int s(x_0+\delta x-x)^* s(x_0-x) \\ &\times\mathrm{e}^{j\frac{2\pi d_{ik}}{\lambda h}\sin\left(\phi_0+\theta_t\right)\cos^2(\phi_0)(x-x_0)}dx. \end{aligned} \tag{14}$$

Recognizing that the exponential term in the above integral leads to the baseline decorrelation described in [6] and that this contribution to decorrelation is small over the range of x considered for short pulses, the term is ignored and (14) can be simplified to

$$\begin{aligned} \mathrm{E}\left\{s_i^* s_k\right\} &= E_t\mathrm{E}\left\{|b|^2\right\}\mathrm{e}^{j\frac{2\pi d_{ik}}{\lambda}\cos\left(\phi_0+\theta_t\right)} \\ &\times\int s(x_0+\delta x-x)^* s(x_0-x)dx. \end{aligned} \tag{15}$$

Again, considering only the case of short pulses, the change in δx with x can be ignored, and the integral can be written as the correlation between a time-delayed version of the pulse and itself. Specifically

$$\begin{aligned} \rho_{ik}(\gamma) &= \int s(x_0+\delta x-x)^* s(x_0-x)dx \\ &= \frac{\int_\tau^\infty f(t-\tau)^* f(t)dt}{\int_0^\infty |f(t)|^2 dt} \end{aligned} \tag{16}$$

where $f(t)$, the nonnormalized pulse shape, is expressed as a function of time and

$$\tau = \frac{2}{c}\sin(\phi_0)\,\delta x = \frac{\lambda}{2\pi c}\gamma \tag{17}$$

where γ is the electrical angle defined by (3).

Therefore,

$$\mathrm{E}\left\{s_k s_i^*\right\} = E_t\mathrm{E}\left\{|b|^2\right\}\mathrm{e}^{-(i-k)\gamma}\rho_{i-k}(\gamma) \tag{18}$$

where d_{ik} in (15) is $(i-k)d$, and it is recognized that $\rho_{ik}(\gamma)$ is defined by the difference $i-k$ (i.e., $\rho_{ik}(\gamma)=\rho_{i-k}(\gamma)$).

Therefore, the correlation matrix of the signal received at the elements of the array (illustrated here by a 3×3 matrix for a three-element array) is

$$\mathbf{R}_s = \begin{pmatrix} 2\sigma_s^2 & 2\sigma_s^2\rho_1(\gamma)\mathrm{e}^{-j\gamma} & 2\sigma_s^2\rho_2(\gamma)\mathrm{e}^{-j2\gamma} \\ 2\sigma_s^2\rho_1(\gamma)\mathrm{e}^{j\gamma} & 2\sigma_s^2 & 2\sigma_s^2\rho_1(\gamma)\mathrm{e}^{-j\gamma} \\ 2\sigma_s^2\rho_2(\gamma)\mathrm{e}^{j2\gamma} & 2\sigma_s^2\rho_1(\gamma)\mathrm{e}^{j\gamma} & 2\sigma_s^2 \end{pmatrix} \tag{19}$$

where $2\sigma_s^2$ is defined as the variance of the complex Gaussian amplitude of the signal, namely $2\sigma_s^2 = E_t E\{|b|^2\}$.

The complete correlation matrix is obtained by adding the diagonal matrix associated with the uncorrelated noise from element to element, and therefore,

$$\begin{aligned} \mathbf{R} &= \mathbf{R}_s + \mathbf{R}_n \\ &= \begin{pmatrix} 2\sigma_s^2+2\sigma_n^2 & 2\sigma_s^2\rho_1(\gamma)\mathrm{e}^{-j\gamma} & 2\sigma_s^2\rho_2(\gamma)\mathrm{e}^{-j2\gamma} \\ 2\sigma_s^2\rho_1(\gamma)\mathrm{e}^{j\gamma} & 2\sigma_s^2+2\sigma_n^2 & 2\sigma_s^2\rho_1(\gamma)\mathrm{e}^{-j\gamma} \\ 2\sigma_s^2\rho_2(\gamma)\mathrm{e}^{j2\gamma} & 2\sigma_s^2\rho_1(\gamma)\mathrm{e}^{j\gamma} & 2\sigma_s^2+2\sigma_n^2 \end{pmatrix} \end{aligned} \tag{20}$$

where $\mathbf{R}_n$ is the noise correlation matrix with diagonal components $2\sigma_n^2$.

Defining the signal-to-noise ratio (SNR) as $2\sigma_s^2/2\sigma_n^2$, the correlation matrix can be rewritten as

$$\mathbf{R} = 2\sigma_s^2\left(1+\frac{1}{\mathrm{SNR}}\right) \times \begin{pmatrix} 1 & \rho_n\rho_1(\gamma)\mathrm{e}^{-j\gamma} & \rho_n\rho_2(\gamma)\mathrm{e}^{-j2\gamma} \\ \rho_n\rho_1(\gamma)\mathrm{e}^{j\gamma} & 1 & \rho_n\rho_1(\gamma)\mathrm{e}^{-j\gamma} \\ \rho_n\rho_2(\gamma)\mathrm{e}^{j2\gamma} & \rho_n\rho_1(\gamma)\mathrm{e}^{j\gamma} & 1 \end{pmatrix} \quad (21)$$

where ρ_n is the correlation coefficient associated with the noise, namely

$$\rho_n = \frac{\mathrm{SNR}}{1+\mathrm{SNR}}. \quad (22)$$

From the correlation matrix $\mathbf{R}$, it is evident that uncorrelated noise from element to element has a different effect on performance than footprint shift. Specifically, the uncorrelated noise results in correlation coefficient ρ_n, which is the same for all pairs of elements. On the other hand, the correlation coefficient for footprint shift is dependent on the element pair spacing. The net result is that pairs with larger spacing are less correlated, and therefore, the incremental increase in angle estimation performance for additional elements drops off (discussed later in Section IV).

Now that the correlation matrix is determined, what remains is to determine a specific function for $\rho_i(\gamma)$. For the results generated in this paper, a signal pulse with an exponential rise and fall is used as this is a good representation of practical sonar pulses. The pulse has the form

$$f(t) = (1-\mathrm{e}^{-at})\mathrm{u}(t) - \left(1-\mathrm{e}^{-a(t-T)}\right)\mathrm{u}(t-T) \quad (23)$$

where T is the time the pulse starts to decay, $\mathrm{u}(t)$ is the unit step function, and a is the inverse of the time constant. As a increases, the pulse approaches a square pulse of duration T. When (23) is applied to obtain $\rho_i(\gamma)$, the following result is obtained:

$$\rho_k(\gamma) = \frac{T-\tau+\frac{\mathrm{e}^{-aT}(\mathrm{e}^{a\tau}+\mathrm{e}^{-a\tau})-2\mathrm{e}^{-a\tau}}{2a}}{T-\frac{(1-\mathrm{e}^{-aT})}{a}} \quad (24)$$

where

$$\tau = \frac{\lambda k\gamma}{2\pi c} \quad (25)$$

and γ is the electrical angle between the closest elements of the array.

To determine the CRLB, the derivative of each term in the correlation matrix $\mathbf{R}$ with respect to the electrical angle γ is required. Considering an arbitrary off-diagonal term, the derivative is

$$\frac{\partial\rho_n\rho_k\mathrm{e}^{jk\gamma}}{\partial\gamma} = \rho_n\left(\rho_k(\gamma)jk\mathrm{e}^{jk\gamma} + \mathrm{e}^{jk\gamma}\rho(\gamma)'\right) \quad (26)$$

where

$$\rho_k(\gamma)' = \frac{\partial\rho_k(\tau)}{\partial\tau}\frac{\partial\tau}{\partial\gamma} = \frac{\left(-2+2\mathrm{e}^{-a\tau}+\mathrm{e}^{-aT}(\mathrm{e}^{a\tau}-\mathrm{e}^{-a\tau})\right)\frac{\lambda k}{2\pi c}}{2\left(T-\frac{(1-\mathrm{e}^{-aT})}{a}\right)} \quad (27)$$

for $\tau < T$.

For a square pulse (i.e., $a \Rightarrow \infty$)

$$\rho_k(\gamma) = 1-\frac{\tau}{T} = 1-\frac{\lambda k\gamma}{2\pi cT} \quad (28)$$

and

$$\frac{\partial\rho_k(\gamma)}{\partial\gamma} = -\frac{\lambda k}{2\pi cT}. \quad (29)$$

For the exponential pulse shape $\rho_k(\gamma)$ is minimized if a is large and the pulse is tending toward a square pulse. Furthermore, $|\rho_k(\gamma)'|$ is a maximum for the square pulse so the closest the relative amplitudes of the two terms in the derivative in (26) can come is

$$\frac{\rho_k(\gamma)k}{|\rho_k(\gamma)'|} \geq \frac{\left(1-\frac{\lambda k\gamma}{2\pi cT}\right)k}{\frac{\lambda k}{2\pi cT}} = 2\pi N_p - k\gamma \geq \pi(2N_p-k) \quad (30)$$

where $N_p = cT/\lambda$ is the number of carrier cycles in the square pulse or the number of carrier cycles in the exponential pulse before it starts to decay. Since the largest value that k can be is $M-1$ where M is the number of elements in the array, and the largest that γ can be is π, the ratio is guaranteed to be larger than an order of magnitude if

$$N_p \geq \frac{M+3}{2}. \quad (31)$$

This inequality holds for all the pulse lengths and array sizes considered in this paper, and therefore, the derivative term involving $\rho_k(\gamma)'$ can be neglected, hence, the off-diagonal terms are approximated by

$$\frac{\partial\rho_n\rho_k\mathrm{e}^{jk\gamma}}{\partial\gamma} \simeq \rho_n\rho_k(\gamma)\,jk\mathrm{e}^{jk\gamma}. \quad (32)$$

With the correlation matrix $\mathbf{R}$ and its derivative defined, the CRLB for the variance of an unbiased estimate of the electrical angle can now be determined. In the next section, the problem of bottom estimation with a two-element array is investigated in detail because these results can be extrapolated to the discussion of the multiple-element problem in Section IV.

III. Two-Element Array and Bottom Estimation

In this section, the accuracy of angle estimation for determining the bottom position is determined for a two-element array. The CRLB for bottom estimation with a two-element array is derived and then compared with simulation results. The differences between the bound and the simulation results are described and explained in the context of measurement accuracy. It is shown that determining the variance of angle estimation estimates is not as straightforward as it seems.

A. CRLB for a Two-Element Array

For a two-element array, the CRLB takes on a fairly simple form as there is only one set of off-diagonal elements in the correlation matrix. Hence, the lack of correlation due to footprint shift can be equated to an equivalent SNR. Specifically, the correlation matrix is

$$\mathbf{R} = 2\sigma_s^2\left(1+\frac{1}{\mathrm{SNR}}\right)\begin{pmatrix} 1 & \rho_n\rho_1(\gamma)\mathrm{e}^{-j\gamma} \\ \rho_n\rho_1(\gamma)\mathrm{e}^{j\gamma} & 1 \end{pmatrix}. \quad (33)$$

Applying (1) and (2) and neglecting the dependence of $\rho_1(\gamma)$ on γ when obtaining the derivative as suggested by (32), the CRLB for the electrical angle γ is

$$\mathrm{CRLB}(\gamma) = \frac{1}{J} = \frac{1 - \rho_n^2 \rho_1(\gamma)^2}{2\rho_n^2 \rho_1(\gamma)^2}. \tag{34}$$

If the product $\rho_n \rho_1(\gamma)$ is treated as a single effective correlation ρ_e, an effective signal-to-noise ratio (SNR_e) is obtained through the relation

$$\mathrm{SNR}_e = \frac{\rho_e}{1 - \rho_e}. \tag{35}$$

The CRLB then becomes

$$\mathrm{CRLB}(\gamma) = \frac{1}{\mathrm{SNR}_e} + \frac{1}{2\mathrm{SNR}_e^2}. \tag{36}$$

For high effective SNR (say above 10), the CRLB can be approximated by

$$\mathrm{CRLB}(\gamma) = \frac{1}{\mathrm{SNR}_e}. \tag{37}$$

Further, for high effective SNR

$$\mathrm{SNR}_e \simeq \frac{1}{\frac{1}{\mathrm{SNR}_n} + \frac{1}{\mathrm{SNR}_1(\gamma)}} \tag{38}$$

where SNR_n and $\mathrm{SNR}_1(\gamma)$ are defined using (35) and substituting ρ_n and $\rho_1(\gamma)$ for ρ_e, respectively. Hence, for high SNR_n, the effective SNR is governed by $\mathrm{SNR}_1(\gamma)$, which is now denoted as SNR_s for notational simplification, therefore,

$$\mathrm{CRLB}(\gamma \,|\, \text{large } \mathrm{SNR}_n) \simeq \frac{1}{\mathrm{SNR}_s}. \tag{39}$$

Equation (39) is valid, of course, only if SNR_s is large, too, but not as large as SNR_n. Specifically, from (28) for a square pulse and (35) and noting that $N_p = cT/\lambda$

$$\mathrm{SNR}_s = \frac{2\pi cT}{\lambda\gamma} - 1 = \frac{2\pi N_p}{\gamma} - 1. \tag{40}$$

For SNR_s to be large, it is required that

$$N_p \gg \frac{\gamma}{2\pi}. \tag{41}$$

So (39) is valid only when the pulse length measured in carrier cycles is very much larger than the spacing measured in wavelength. If this condition is true and the signal-to-noise ratio (SNR_n) increases, the CRLB limits at the level $1/\mathrm{SNR}_s$. This limit for square pulses is

$$\mathrm{CRLB}(\gamma \,|\, \text{square pulse}) = \frac{1}{\frac{2\pi N_p}{\gamma} - 1} \simeq \frac{\gamma}{2\pi N_p}. \tag{42}$$

Fig. 3 illustrates the behavior of the two-element CRLB for increasing SNR, a 50-cycle pulse, and an electrical angle of 60°. For this figure, the value of a for the exponential pulse, describing the rise time, was equated to the exponential envelope of an underdamped second-order circuit

$$a = \frac{2\pi f}{2q} \tag{43}$$

where it is assumed that the operating frequency f is the resonant frequency of the second-order circuit and q is the quality factor. This value of a means that the pulse reaches 95.7% of its maximum value within q cycles of the carrier. As q decreases, the exponential pulse approaches a square envelope and the resulting CRLB matches that of a square pulse, which in the limit for high SNR, is represented by the thin solid line.

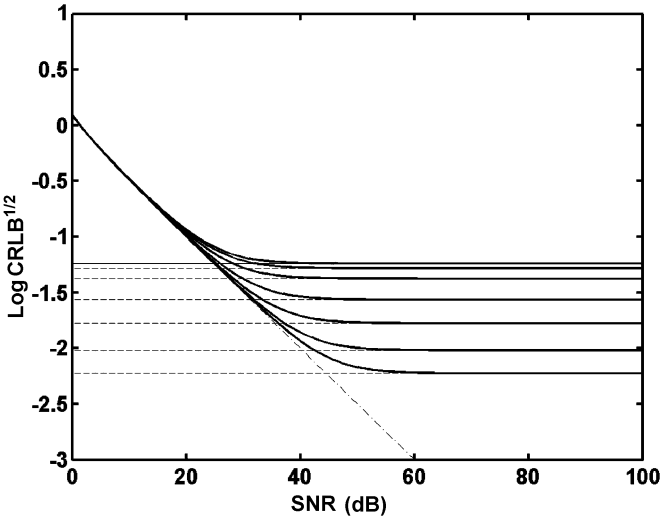

Fig. 3. The two-element CRLB expressed as $\log \mathrm{CRLB}^{1/2}$, where $\mathrm{CRLB}^{1/2}$ has the unit of radians, as a function of SNR. The pulse length is 50 cycles, the frequency is 100 kHz, and the electrical angle is 60°. The dash–dot line is the CRLB for uncorrelated noise alone. The dashed lines are the limits imposed by footprint shift in the absence of uncorrelated noise for pulses with q's of 0.1, 0.3, 1, 3, and 10, top to bottom. The solid thin line is the limit for a square pulse. The thick solid lines are the associated CRLBs for both uncorrelated noise and footprint shift together.

This figure shows the CRLB decreasing for increasing SNR (thin dash-dot line). However, once the SNR reaches the point associated with the footprint shift, namely SNR_s, the CRLB plateaus and no longer decreases with increasing SNR. The plateau level is described by the dashed thin lines for various values of q describing the rise time of the 50-cycle pulse. By gradually blurring both the leading and trailing edges of the pulse (i.e., higher q), the effect of the footprint shift is reduced, and therefore, the plateau is lower. But nevertheless, according to the CRLB, the angle estimation ability limits at that associated with SNR_s regardless of further decreases in SNR_n.

Fig. 4 illustrates the behavior of the CRLB as a function of the electrical angle for given signal-to-noise ratios and a $q = 3$. The major feature of this plot is that the CRLB decreases as the electrical angle approaches zero (i.e., signal is coming from broadside). For this angle, there is no footprint shift noise (i.e., $\mathrm{SNR}_s = \infty$), so the CRLB is determined by SNR_n only. Off broadside, the CRLB is determined by both SNR_s and SNR_n, assuming the value associated with the lowest if there is a large difference. For example, at low SNR_n (e.g., the 10 dB curve) the CRLB is determined by SNR_n because it is much lower than SNR_s and the CRLB is independent of the electrical angle. The thin solid line is the CRLB for a 50-cycle square pulse with no noise present (i.e., $\mathrm{SNR}_n = \infty$) and is shown for reference.

The major conclusion from this analysis of the CRLB for a two-element array is that footprint shift limits how well one can expect to estimate the electrical angle and, hence, the arrival angle. This limit decreases as the pulse length increases or the q increases, but these increases tend to decrease the resolution along the bottom.

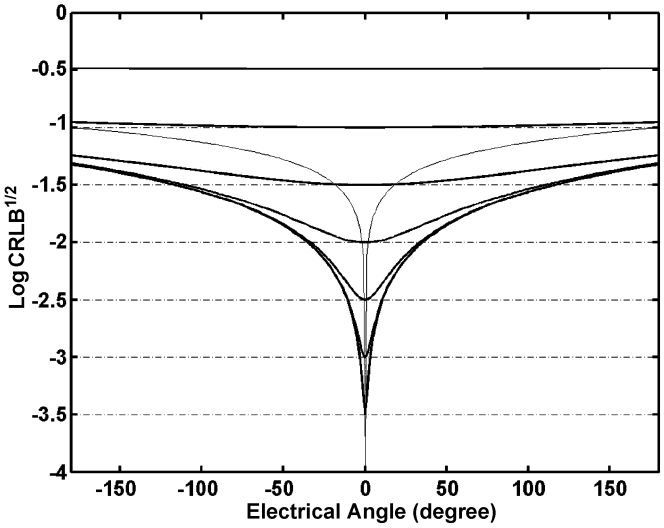

Fig. 4. The two-element CRLB expressed as $\log \mathrm{CRLB}^{1/2}$, where $\mathrm{CRLB}^{1/2}$ has the units of radians, as a function of electrical angle. The pulse length is 50 cycles, the frequency is 100 kHz, and the q is 3. The dash–dot lines are the CRLBs for uncorrelated noise alone for signal-to-noise ratios of 10, 20, 30, 40, 50, 60, and 70 dB, top to bottom. (The 10 dB dash–dot line is hidden behind the solid line.) The thin solid line is the footprint shift limit for a square pulse in the absence of uncorrelated noise. The thick solid lines are the CRLBs for uncorrelated noise and footprint shift together for the associated SNR.

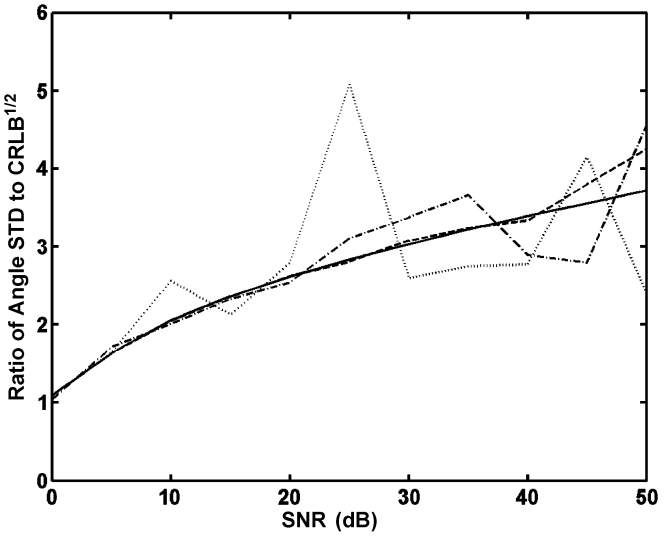

Fig. 5. The ratio of the standard deviation of the electrical angle to $\mathrm{CRLB}^{1/2}$ as a function of the SNR (thick solid line). Dotted line represents the ratio of the sample standard deviation to $\mathrm{CRLB}^{1/2}$ for 100 trials, dash–dot line represents 1000 trials, and dashed line represents 100 000 trials.

The next step in establishing the accuracy of angle measurements is to determine if the CRLB is actually a good representation of how well the angle can be determined. The CRLB is a bound on the variance of an unbiased estimator, but there is no guarantee that the bound can actually be attained. Angle estimation is intrinsically nonlinear, and therefore, establishing closeness to the CRLB is difficult especially for low sample support. Bottom estimation must be accomplished with a few samples to maintain resolution, and therefore, asymptotic closeness to the CRLB is of little use even if it can be proven analytically.

One indication that the CRLB might be a reasonable base to work from is shown by comparing the bound with simulation results. This procedure involves programming a simulator to produce the same signal statistics as the model suggests and determining the sample variance of the estimator and comparing that to the CRLB. This procedure works if it can be established that the sample variance is actually a good representation of the real variance of the estimator. Usually, a certain large number of trials (for example 100 as employed in [5]) are performed in hopes that the variance will be well estimated. However, the goodness of the variance estimator depends to a large degree on the underlying probability density of the angle estimations. In what follows, it is shown that for a single snapshot of a two-element array, the sample variance is typically a poor representation of the real variance.

Part of the reason for investigating the single snapshot in detail is that a probability density for the angle estimator is known, and therefore, the true variance can be determined. Furthermore, the problems associated with a single snapshot shed light on problems likely to be encountered with multiple snapshots and multiple array elements.

An estimator of the electrical angle or phase shift between two array elements is the angle of the complex quantity $s_1^* s_2$. This angle has the probability density [6], [8]

$$p(\gamma) = \frac{1-\rho^2}{2\pi(1-\beta^2)^{\frac{3}{2}}}\left[\beta \arcsin(\beta) + \frac{\pi\beta}{2} + \sqrt{1-\beta^2}\right] \tag{44}$$

where $\beta = \rho\cos(\gamma - \overline{\gamma})$, ρ is the correlation between the two complex Gaussian random variables, and $\overline{\gamma}$ is the mean phase shift. This probability density differs greatly from the normal density, although it does have a characteristic bell shape. The first difference to be noted in passing is that the angle probability density must be understood as being modulo 2π, so for large variances, comparing with the normal density is meaningless. For small variances, the angle probability density has much larger tails than the normal density, and the remaining probability is more tightly grouped around the mean.

As a result of the nature of the angle probability density, it can be expected that the variance is difficult to estimate accurately even with a large number of trials. The larger tails of the density results in low probability events contributing significantly to the variance and, therefore, the number of trials has to be large enough to capture the behavior of these events. Fig. 5 illustrates this effect by plotting the ratio between the true standard deviation [calculated numerically using (44)] and the square root of the CRLB as a function of the SNR. Also plotted is the ratio between the estimated standard deviation and the square root of the CRLB for 100, 1000, and 100 000 trials.

The general character of the estimated ratio is that it follows the true value to a certain SNR and then breaks off at that level and fluctuates rather wildly after that. The explanation is that as the SNR increases, the angle probability density function gets narrower, but the tails are still significant. Therefore, as the SNR increases, the large variations become less probable, but they still contribute significantly to the variance. Hence, a larger number of trials is required to capture the true variance as the SNR increases.

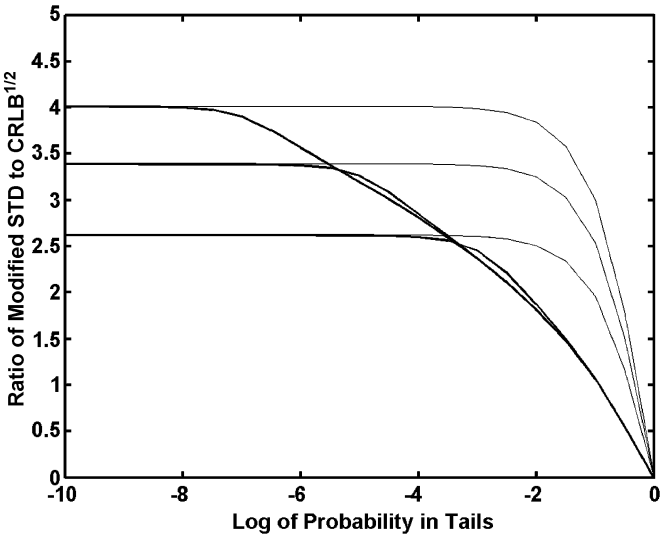

Fig. 6. Ratio of modified standard deviation (calculated with the part of the density closest to the mean) to $\mathrm{CRLB}^{1/2}$. The horizontal axis is the log of the probability left out of the calculation of the standard deviation. The thick lines are for the angle density and the thin lines for a Gaussian density with equivalent variances. The curves are for signal-to-noise ratios of 60, 40, and 20 dB, top to bottom.

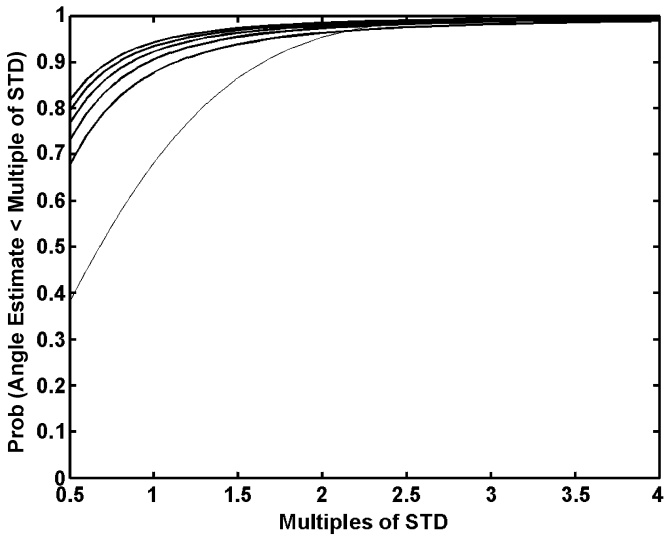

Fig. 7. Probability that the estimate will be less than so many standard deviations from the mean. Thick solid curves are for the angle probability density and signal-to-noise ratios 60, 50, 40, 30, and 20 dB, top to bottom. For reference, the thin solid line is a similar calculation for a Gaussian probability density.

Fig. 6 shows the ratio of standard deviation to the square root of the CRLB where the calculation of the standard deviation is over the inner part of the probability density function (i.e., that part closest to the mean). The horizontal axis is the amount of probability left out of the calculation (i.e., the probability in the upper and lower tails). The horizontal axis can be viewed as being roughly the inverse of the number of trials required to obtain the given level (note the log scale). The thick black curves are for the angle density and represent signal-to-noise ratios of 20, 40, and 60 dB, lower curve to higher. For comparison, the black thin curves are for the normal density with an equivalent variance. For the highest SNR shown, 60 dB, to approximate the true ratio, the tail probability excluded must be less than about 10^{-7} for the angle density, while for the normal density, the tail probability excluded is only 10^{-2}. Taking these probabilities as approximately the inverse of the number of trials required, 10^7 or greater trials are required to effectively estimate the standard deviation for the angle density, compared with only 100 for the normal density with equivalent variance.

From a practical point of view, the sample variance will continue to increase as the number of trials increases until a large enough number of trials (and this is very large for reasonable signal-to-noise ratios) is reached. Therefore, determining the variance of the estimator through the simulation approach can lead to significant problems and/or misleading results. For example, consider the case of using 100 trials to measure the sample variance. For this case, the probability is 1/100, which yields a ratio to the CRLB in the region of -2 on the x-axis of Fig. 6. Since the resulting ratio in this region for the angle density is around 2 for all the SNR curves, it might be concluded that the standard deviation is twice the square root of the CRLB. This conclusion would be wrong, of course, but there is no evidence of it being so unless fewer and more trials are employed to confirm, and in this case not confirm, the validity of the estimate.

It should be noted that the curves in Fig. 6 are rough estimates only of what the sample variance might be. Indeed, it is expected that in determining the sample variance, there will be outliers that will bias the estimate upward. Therefore, these curves should be considered to be slightly lower than the true sample variance.

Perhaps a better approach to the problem, at least for the single snapshot case where we have the probability density function, is to represent performance by probability bounds instead of variance. One of the properties of the angle pdf that makes this approach attractive is that much of the probability is close to the mean implying that for a single sample, there is a high probability that the angle will be close to the mean. So for a given SNR, a probability that a sample will be within so many degrees of the mean can be determined.

Specifically, referring to Fig. 7 where the probability of the angle estimate being less than so many standard deviations from the mean is shown, it is evident that the initial probabilities are higher than those for the normal probability density function and vary with the SNR. In estimating the electrical angle, it can be said that for a reasonably high SNR, the estimate will be within approximately one standard deviation 90% of the time, while for the normal density, it is only 68% of the time.

Practically, the curves in Fig. 7 show that angle estimates will generally be more tightly grouped around the means than if they were distributed normally with the same variance, but there will be outliers that are required to make the variances equal. So although the true variance might be significantly larger than the CRLB, a large percentage of the estimates may well be within the standard deviation described by the bound.

The density describing the angle estimates for one snapshot is particularly interesting in this regard. In Fig. 7, the probability is plotted as a function of multiples of the standard deviation. If probability is plotted as a function of multiples of the standard deviation described by the CRLB (i.e., $\mathrm{CRLB}^{1/2}$), the result

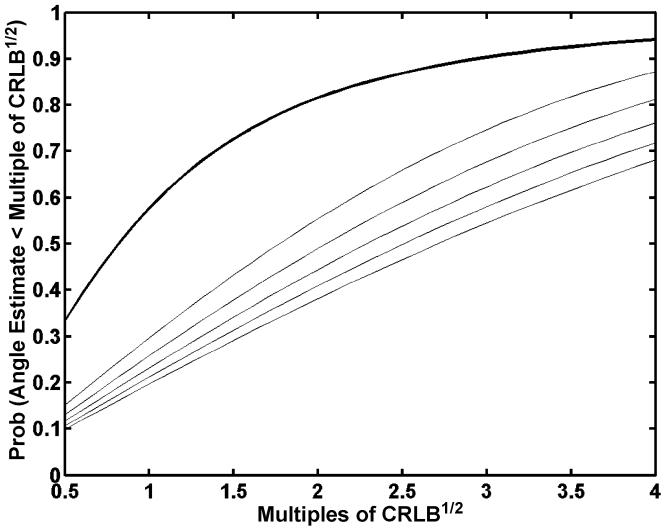

Fig. 8. Probability that the estimate will be less than so many multiples of the $\mathrm{CRLB}^{1/2}$. Thick solid curve is for the angle probability density for the signal-to-noise ratios 60, 50, 40, 30, and 20 dB. (They lie on top of one another.) For reference, the thin lines are for a Gaussian probability density with the same signal-to-noise ratios, top to bottom.

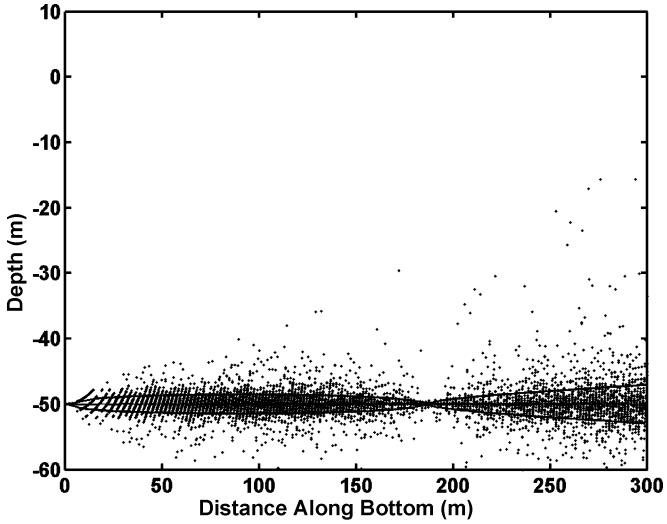

Fig. 9. Scatter plot of bottom estimates obtained through simulation for a two-element array with a separation of 2λ, a square pulse, and for footprint shift only. The frequency is 100 kHz, the tilt angle 15°, the pulse length 50 cycles, and the depth 50 m. The solid lines represent $\pm 2 \times \mathrm{CRLB}^{1/2}$ about the position of the flat bottom. The bottom is simulated by circular symmetric Gaussian scatterers placed uniformly random over the bottom with an average density of 200 scatterers per meter.

shown in Fig. 8 is obtained. In other words, the probability of being within a multiple of the standard deviation described by the CRLB is independent of the SNR if the SNR is reasonably high, say above 20 dB. Note that the curves for the normal density are now dependent on the SNR.

The reason that the probability of being within a multiple of the $\mathrm{CRLB}^{1/2}$ is independent of the SNR follows from the function describing the probability density function for a high SNR. The probability density function for high SNR near the mean can be approximated by

$$f_\gamma(\gamma) \simeq \frac{\mathrm{SNR}^{\frac{1}{2}}}{(2+\mathrm{SNR}\gamma^2)^{\frac{3}{2}}} \tag{45}$$

and when scaled to multiples of the $\mathrm{CRLB}^{1/2}$ for high SNR, namely $n = \gamma \mathrm{SNR}^{1/2}$ since the $\mathrm{CRLB}(\gamma \,|\, \text{high SNR}) = 1/\mathrm{SNR}$, the approximation to the density becomes

$$f_n(n) \simeq \frac{1}{(2+n^2)^{\frac{3}{2}}} \tag{46}$$

which is independent of the SNR.

This function resembles the Student's t-distribution with two degrees of freedom, but it is obviously not the Student's t-distribution because the interval for that density is the entire real line, whereas the interval here is $\pm\pi$ at most. Strictly speaking, the density resembles that of a Student's t-distribution near the mean only. For high SNR, this interval (near the mean) contains most of the probability. Moreover, the variance for a Student's t-distribution with two degrees of freedom is infinite, which is certainly not the case here because the variance is bounded by the integration limit of $\pm\pi$.

Therefore, by employing the equations describing the CRLB for high SNR [(38) and (39)], probability bounds for the error are obtained from Fig. 8. Specifically, errors in the electrical angle estimates will be less than two times the standard deviation described by the CRLB 81% of the time.

A specific example of bottom estimation is displayed in Fig. 9. This figure also shows the standard deviation limit described by $2 \times \mathrm{CRLB}^{1/2}$. For this figure, the two-element array was tilted at 15°, the frequency was 100 kHz, the element separation was 2λ, the pulse was square with a length of 50 carrier cycles (same parameters as the square pulse example in [5]), and there is no noise (i.e., $\mathrm{SNR}_n = \infty$). The bound and scatter error go to zero at a distance along the bottom of 187 m because at this range, the footprint shift noise is zero because the bottom is broadside the array elements, which are tilted at 15°.

Fig. 10 shows the estimated standard deviation of the electrical angle as a function of distance along the bottom. The estimate of the standard deviation was made utilizing 100 trials, and therefore, from Fig. 6, it is expected that the estimated standard deviation will be close to $2 \times \mathrm{CRLB}^{1/2}$, and indeed it is.

Figs. 9 and 10 show the spread in bottom estimation resulting from footprint shift only. If uncorrelated noise is present, the spread will be affected accordingly. To illustrate the effect of uncorrelated noise, noise was added to the simulated signals to produce an SNR versus distance-along-the-bottom curve shown in Fig. 11. The thick solid line in the figure is the SNR calculated using the sonar equation and the associated average scattering strength and pulse length. The thin solid line is the SNR estimated from the signal produced by the simulator. As is typical with real deployments, the SNR is high at close ranges and then drops off due to spherical spreading and decreased bottom footprint of the pulse at farther ranges. Therefore, it is expected that the dominant error source will be the footprint shift at small ranges changing to uncorrelated noise at large ranges.

Figs. 12 and 13 show the spread associated with both footprint shift and uncorrelated noise. Comparing Fig. 9 where only footprint shift is present with Fig. 12, it is evident that the spread at small ranges does indeed follow that of the footprint shift model,

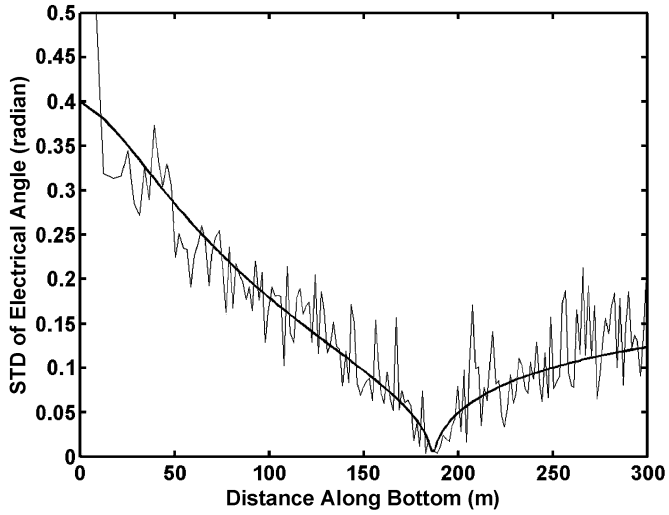

Fig. 10. Sample standard deviation for 100 trials as a function of distance along the bottom for the simulated data for footprint shift only shown in Fig. 9 (thin solid line). The thick solid line is the standard deviation predicted using $2 \times \mathrm{CRLB}^{1/2}$.

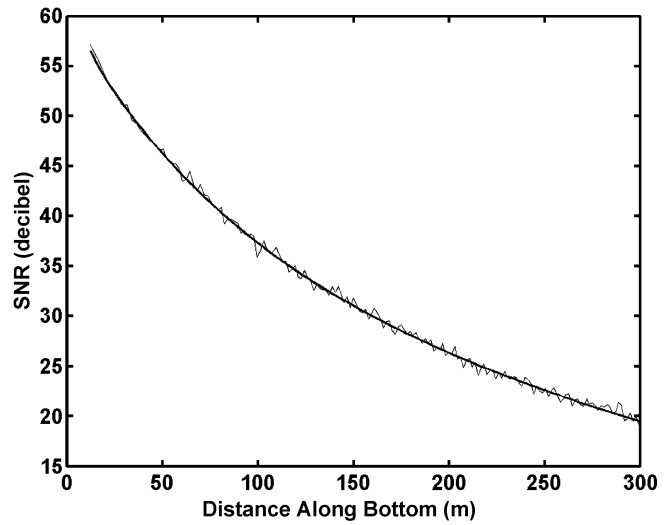

Fig. 11. Single-element SNR for uncorrelated noise added to the simulation signal of Fig. 10 as a function of distance along the bottom. The thick solid line is the SNR predicted from the sonar equation. The thin solid line is the estimated SNR from simulated data.

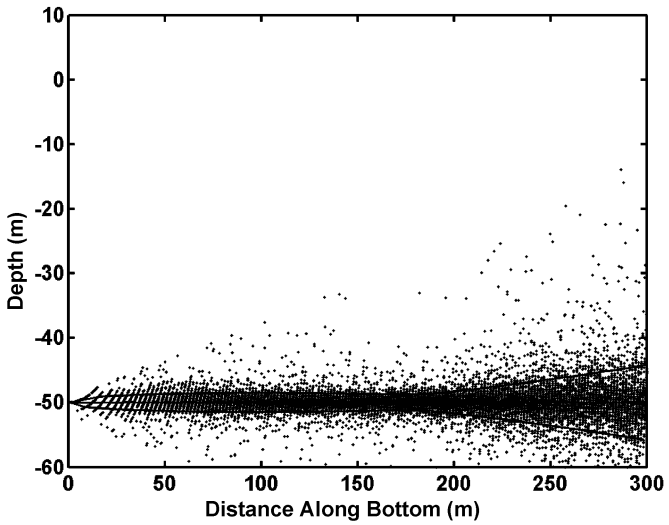

Fig. 12. Scatter plot of bottom estimates for both footprint shift and uncorrelated noise for the same simulation condition as those for Fig. 10. The thick solid lines represent $\pm 2 \times \mathrm{CRLB}^{1/2}$ about the actual bottom position.

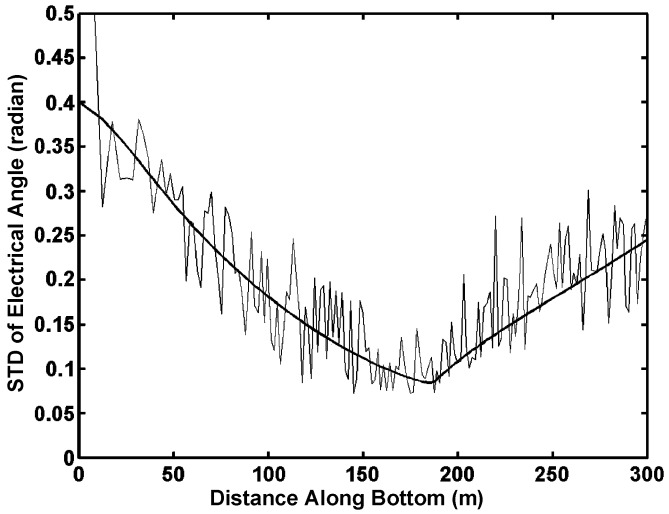

Fig. 13. Sample standard deviation for 100 trials as a function of distance along the bottom for the simulated data for both footprint shift and uncorrelated noise shown in Fig. 12 (thin solid line). The thick solid line is the standard deviation predicted using $2 \times \mathrm{CRLB}^{1/2}$.

while at larger ranges, the spread is dominated by the uncorrelated noise. The solid lines in Fig. 12 are the $2 \times \mathrm{CRLB}^{1/2}$ predictions. Fig. 13 shows the standard deviation for the combined footprint shift and uncorrelated noise error sources. The thick solid curve is the $2 \times \mathrm{CRLB}^{1/2}$ prediction for 100 trials of the simulation. These curves are to be compared with those of Fig. 10. Again, it is evident that as the SNR drops and the uncorrelated noise begins to dominate, the spread increases over that due to the footprint shift alone. Specifically, the null in the spread due to footprint shift at a distance of 187 m is filled in by the spread caused by uncorrelated noise.

B. Multiple Snapshots

In this section, the improvement in angle estimation obtained by using multiple snapshots is discussed. For swath bathymetry applications, the multiple snapshots are usually obtained from a single ping, and therefore, they are spread in range as shown in Fig. 14. A series of array snapshots is taken centered on the time the angle estimate is desired. For analysis in this paper, it is assumed that the snapshots are taken far enough apart that they are uncorrelated. This assumption allows the CRLB to be calculated from the sum of the Fisher information for each snapshot. Practically, this assumption means that there is no overlap between pulse footprints on the bottom, and therefore, the snapshots must be separated by at least a pulse length.

This assumption of uncorrelated snapshots is reasonable in the sense that if the snapshots are too closely spaced, no new information is obtained and the estimation accuracy of a single snapshot is obtained. Reducing the correlation provides new information and, hence, improved estimation, provided secondary angle estimation clues are not available.

1) Pre-Estimation and Post-estimation Averaging: There are two basic techniques available for combining multiple

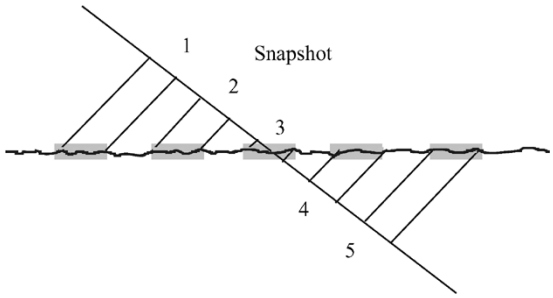

Fig. 14. Geometrical configuration for obtaining independent snapshots about a central position on the bottom from one ping.

snapshots to obtain an angle estimate. The first is to estimate the angle for each snapshot and then average to obtain the final estimate. This technique is called post-estimation averaging. The second consists of averaging the products $s_1^* s_2$ for each snapshot and then estimating the angle from the complex components of that average. This technique is called pre-estimation averaging. This second technique is better than the first in certain circumstances, as briefly outlined below.

For post-estimation averaging, the variance of the estimator is simply the sum of the variances of the single snapshot estimations. If the snapshots are close enough to each other, the variance may be considered approximately equal, and averaging results in a reduction of the estimation variance by a factor of N, which is the number of snapshots. Similarly, the CRLB is reduced by a factor of N because the Fisher information is multiplied by N. Therefore, the ratio of the estimator's variance to the CRLB remains constant at the value for a single snapshot, although the estimator's variance decreases by a factor of N.

The situation is quite different for pre-estimation averaging. For this case, the approximate ratio of the estimator's variance to the CRLB for high signal-to-noise ratios is determined in Appendix II and is

$$\frac{\mathrm{var}(\hat{\gamma})}{\mathrm{CRLB}(\gamma)} \simeq \frac{N}{N-1}, \quad N > 1. \tag{47}$$

Therefore, for pre-estimation averaging, the variance of the estimator approaches the CRLB as N increases. The two cases are compared in Fig. 15, where the ratio of the standard deviation of the estimate to the square root of the CRLB for an SNR of 20 dB is plotted as a function of N. The thin and thick solid lines are the predicted ratios for post- and pre-estimation averaging, respectively. The circles (post-estimation averaging) and stars (pre-estimation averaging) are simulated results for the two cases. It can be seen that the ratios for both cases follow the predicted curves with the ratio for pre-estimation averaging approaching one for increasing N.

From Fig. 15 and (47), it is concluded that the number of snapshots processed does not have to be very large before the CRLB is achieved for practical purposes. Indeed, most of the gain is obtained in the first five snapshots for which the ratio for the variances is 1.25 and the ratio for the standard deviations is $\sqrt{1.25} = 1.118$. Specifically, the test statistic becomes essentially Gaussian for increasing numbers of snapshots, and therefore, the CRLB is a reliable estimate of the variance.

Although pre-estimation averaging seems to have a decided advantage over post-estimation averaging, post-estimation averaging should not be too quickly dismissed. The performance of pre-estimation averaging is greatly affected by the validity of assumptions made concerning the underlying random variables. The gain achieved in Fig. 15 assumes that the snapshots are drawn from identical distributions. If one of the snapshots is large compared to the others, it will dominate the average and the resulting variance will be close to that for a single snapshot. post-estimation averaging does not suffer from this effect because one angle will not dominate another in the same way. Therefore, post-estimation averaging is more robust in unequal snapshot situations. This effect will be illustrated presently.

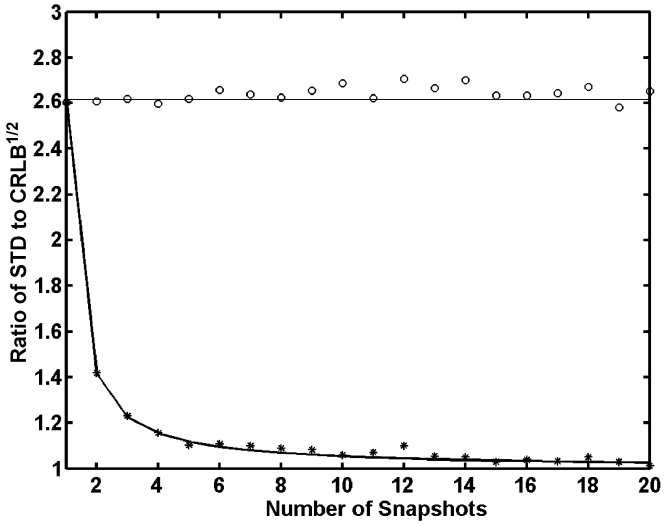

Fig. 15. Ratio of standard deviation to $\mathrm{CRLB}^{1/2}$ for pre-estimation averaging (thick solid line) and post-estimation averaging (thin solid line) as a function of the number of snapshots. The stars are simulation results for pre-estimation averaging and the open circles simulation results for post-estimation averaging for 100 trials.

2) Bottom Estimation Performance With Pre-estimation Averaging: To demonstrate the improvement obtained in the bottom estimate by using multiple snapshots a simulation was run with parameters the same as for Figs. 9 and 10. Figs. 16 and 17 are the corresponding figures with five snapshots averaged to yield the bottom estimate. In creating these figures, the snapshots were generated from new trials and, therefore, not from the same ping. In practice, this would mean that the data from different pings were averaged together, which is not practical as it greatly decreases along track resolution. However, it is useful in the investigation of the utility of multiple snapshots.

Comparing Fig. 9 for one snapshot with Fig. 16 for five snapshots (pre-estimation averaging), it is seen that the $2\times\mathrm{CRLB}^{1/2}$ curves are tighter by a factor of $\sqrt{5} = 2.236$ (note the vertical scale change). But more importantly, there is not as much scatter beyond these bounds. As predicted pre-estimation averaging of snapshots reduces scatter and improves the bottom estimate.

Comparing Fig. 10 for one snapshot with Fig. 17 for five snapshots, there is again a decrease in the standard deviation by a factor of 2.236 over the results for a single snapshot. Specifically, the $2 \times \mathrm{CRLB}^{1/2}$ curve drops from a maximum of 0.4 to a maximum of 0.179. For pre-estimation averaging, the variance drops more than this and is shown by the thick solid simulation curve, which is very close to that of the $\mathrm{CRLB}^{1/2}$, and matches the dashed curve, which is $1.118\times\mathrm{CRLB}^{1/2}$, the ratio

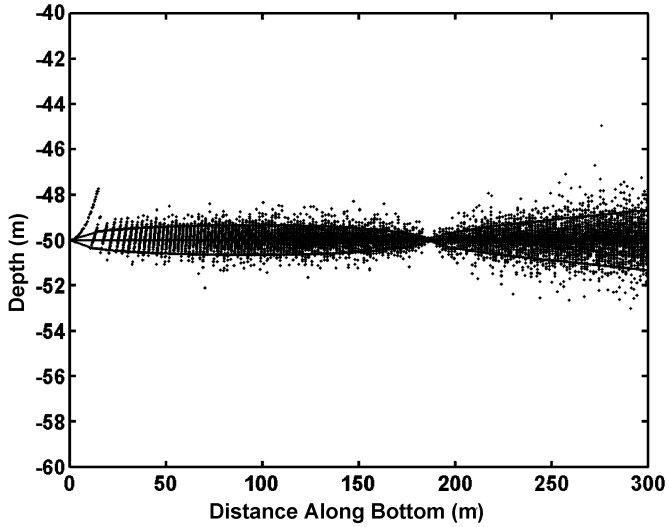

Fig. 16. Scatter plot of bottom estimates for footprint shift only for five snapshots using pre-estimation averaging and the same simulation parameters as for Fig. 9. The thick solid line is the standard deviation predicted using $\pm 2 \times \mathrm{CRLB}^{1/2}$.

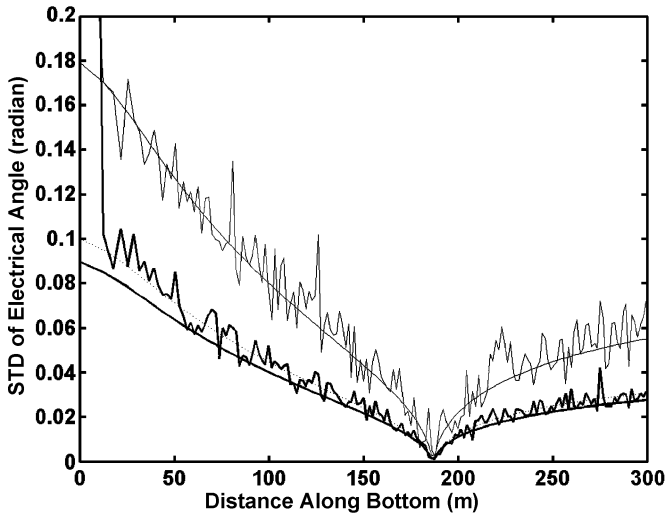

Fig. 17. Sample standard deviation for 100 trials and 5 snapshots for footprint shift alone and the same simulation situation as Fig. 10. The dashed line represents $1.118 \times \mathrm{CRLB}^{1/2}$ and the thick solid smooth line $\mathrm{CRLB}^{1/2}$. The smooth thin solid line is $2 \times \mathrm{CRLB}^{1/2}$. The thick solid rough line is the sample standard deviation for pre-estimation averaging and the thin solid rough line for post-estimation averaging. The five snapshots are taken from different simulated pings.

expected from Fig. 15 and averaging five snapshots. The simulation curve shown with a thin line is for post-estimation averaging, and it follows the $2 \times \mathrm{CRLB}^{1/2}$ curve as expected. Therefore, the gains expected from the curves shown in Fig. 15 comparing post and pre-estimation averaging are indeed realized for combining snapshots obtained from separated pings.

If the snapshots are obtained from the same ping as illustrated in Fig. 14, the statistics of the snapshots are expected to be similar away from nadir, and therefore, results similar to those in Fig. 17 are expected for this condition. Fig. 18 shows the results for five snapshots averaged over 100 trials where the five snapshots are chosen for each bottom point from neighbors in the same ping. These neighboring snapshots are separated by twice the pulse length, which is 50 cycles at a carrier frequency of

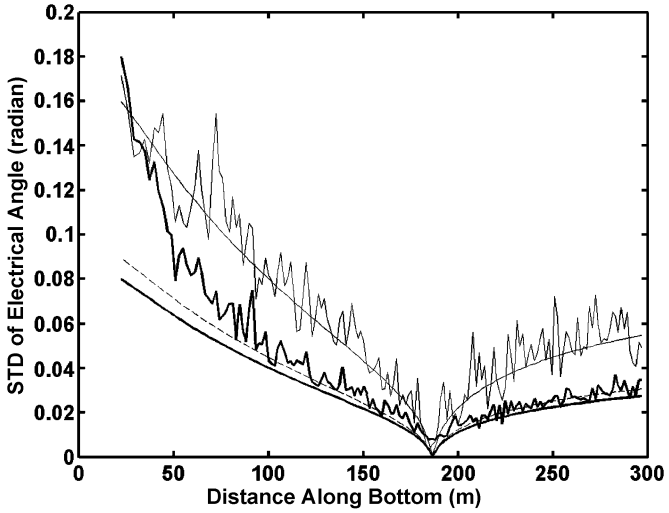

Fig. 18. Sample standard deviation for 100 trials and 5 snapshots as described in Fig. 17, but now, the snapshots are taken from different positions in the same ping.

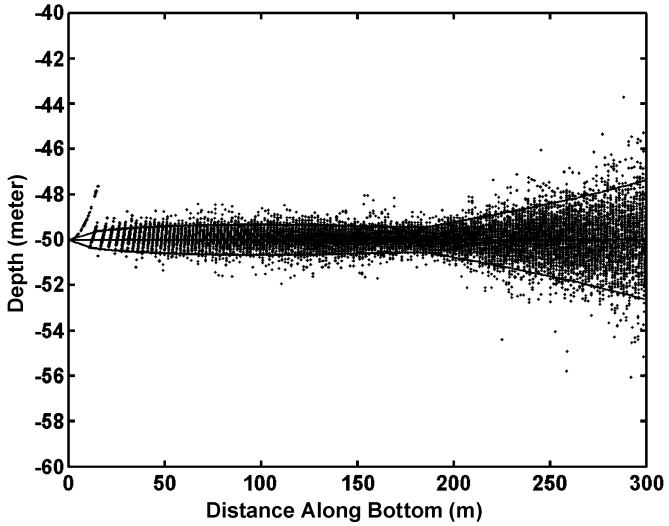

Fig. 19. Scatter plot of the bottom position for five snapshots and the same situation as Fig. 16, but with uncorrelated noise added with a single-element SNR as shown in Fig. 11.

100 kHz. The $\mathrm{CRLB}^{1/2}$, $1.118 \times \mathrm{CRLB}^{1/2}$, and $2 \times \mathrm{CRLB}^{1/2}$ curves are shown along with the simulation results for pre-estimation averaging (thick solid rough curve) and post-estimation averaging (thin solid rough curve). The results for post-estimation averaging follow the $2 \times \mathrm{CRLB}^{1/2}$ curve as before (Fig. 17), but the result for pre-estimation averaging rises above the $1.118 \times \mathrm{CRLB}^{1/2}$ curve as nadir is approached. This rise is due to the imbalance in signal strengths associated with the five snapshots in the nadir region. The post-estimation averaging simulation curve is unaffected because the estimation procedure mitigates the amplitude imbalance.

If uncorrelated noise is present, the trends for multiple snapshots are very similar to those for a single snapshot. Figs. 19 and 20 show the results for five snapshots resulting from the same SNR curve shown in Fig. 11. Again, at small ranges, the spread is dominated by the footprint shift effect and the spread at large ranges is dominated by the uncorrelated noise. The factors of

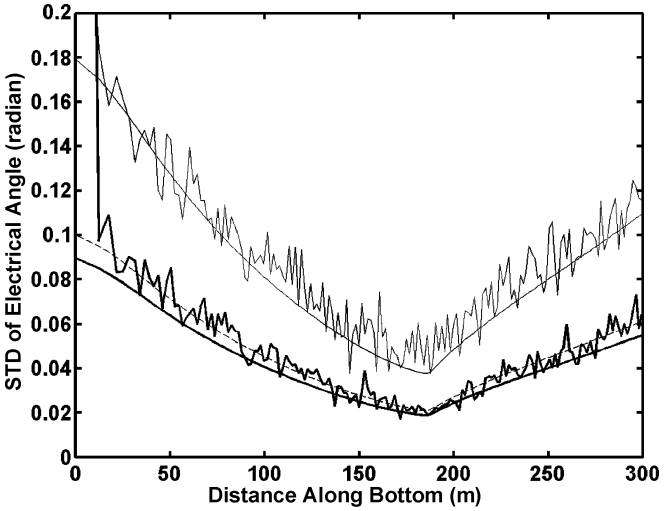

Fig. 20. Sample standard deviation for 100 trials and 5 snapshots as described in Fig. 17, but now including the effect of uncorrelated noise. The single-element SNR is shown in Fig. 11.

$1.118 \times \mathrm{CRLB}^{1/2}$ and $2 \times \mathrm{CRLB}^{1/2}$ for pre-estimation averaging and post-estimation averaging respectively hold for both footprint shift and uncorrelated noise.

Although it is tempting to recommend the use of pre-estimation averaging because its performance approaches the CRLB for the model under consideration, post-estimation averaging may be better in situations where imbalances in snapshot statistics occur. An example of such a situation is a bottom that is made up of a few dominant scatterers mixed with many lower amplitude scatterers.

IV. Multiple Array Elements and Bottom Estimation

In the previous section, discussion focused on the ability to estimate the bottom using signals from a two-element array. In this section, the analysis is extended to arrays consisting of more than two elements. There are at least three good reasons for extending the number of elements in the array. The first is that with additional elements, more angles can be estimated for a given snapshot or group of snapshots. With two elements, only one angle can be estimated, and therefore, if there are competing signals from different directions, say a direct signal from the bottom and a first-surface-bounce multipath, the estimate of the bottom angle is compromised. For arrays composed of M elements, up to $M-1$ angles can be estimated due to an increase in the number of degrees of freedom. Tradeoffs in how these degrees of freedom are used are outlined in [3] and [4].

The second reason for extending the number of elements is to mitigate the effects of array imperfections. Crosstalk between elements and acoustic interactions with the structure of the housing influence accuracy of angle estimates. The effect of these characteristics of practical arrays can often be reduced by the averaging that takes place in the processing of multi-element array signals [9].

Finally, the third reason for employing multiple elements is that there is a gain in estimation accuracy to be had in the presence of uncorrelated noise from element to element. Therefore, there is a gain over front-end thermal noise and other like noise sources. This gain will be described presently.

The number of processing schemes that can be employed, each with its own advantages and disadvantages, complicates describing the bottom estimation performance of multiple-element arrays. For an extensive review of these schemes, the reader is referred to [7]. In this paper, the CRLB is employed to evaluate potential performance and to establish trends in order to steer clear of estimation method issues.

The gain achieved over uncorrelated noise from element to element follows from the autocorrelation matrix $\mathbf{R}$ as shown in (21) for a three-element array. If only uncorrelated noise is present (i.e., the signal is perfectly correlated), the autocorrelation matrix simplifies to

$$\mathbf{R} = 2\sigma_s^2\left(1+\frac{1}{\mathrm{SNR}}\right)\begin{pmatrix} 1 & \rho_n \mathrm{e}^{-j\gamma} & \rho_n \mathrm{e}^{-j2\gamma} \\ \rho_n \mathrm{e}^{j\gamma} & 1 & \rho_n \mathrm{e}^{-j\gamma} \\ \rho_n \mathrm{e}^{j2\gamma} & \rho_n \mathrm{e}^{j\gamma} & 1 \end{pmatrix}. \tag{48}$$

For this autocorrelation matrix and the assumption of Gaussian statistics for both the signal and the noise, it is shown in [7, p. 946] that the CRLB is

$$\mathrm{CRLB}(\gamma) = \frac{1}{N}\left(\frac{6}{M(M^2-1)\mathrm{SNR}_n} + \frac{6}{M^2(M^2-1)\mathrm{SNR}_n^2}\right) \tag{49}$$

where N is the number of snapshots, M is the number of array elements, and SNR_n is the SNR. (It should be noted that this bound is independent of the actual electrical angle γ). The second term in the brackets dominates at low signal-to-noise ratios and the first at high signal-to-noise ratios. Since the discussion in this paper focuses on high SNR situations, the CRLB is approximated by the first term, namely

$$\mathrm{CRLB}(\gamma) \simeq \frac{6}{NM(M^2-1)\mathrm{SNR}_n} \tag{50}$$

for signal-to-noise ratios above say 20 dB.

Since the CRLB for two elements at high SNR is $1/(N\mathrm{SNR}_n)$, the CRLB for multiple elements is smaller than the two-element bound by the ratio

$$\frac{\mathrm{CRLB}(\gamma)}{\mathrm{CRLB}_2(\gamma)} = \frac{6}{M(M^2-1)} \tag{51}$$

where $\mathrm{CRLB}_2(\gamma)$ is the CRLB for a two-element array. This ratio shows that there are merits to increasing the number of array elements when uncorrelated noise from element to element is the issue. There are, of course, practical limits to the size of arrays but even small arrays achieve significant gains.

The feature of the autocorrelation matrix that makes this gain possible is that the correlation remains constant regardless of element spacing. If the correlation did drop off for larger spacings, including the signals from these spacings does not have the same advantage. For example, consider the correlation matrix in (21) again, but now let $\rho_n \Rightarrow 1$ (i.e., $\mathrm{SNR}_n \Rightarrow \infty$). For this situation, the following matrix is obtained:

$$\mathbf{R} = 2\sigma_s^2\begin{pmatrix} 1 & \rho_1(\gamma)\mathrm{e}^{-j\gamma} & \rho_2(\gamma)\mathrm{e}^{-j2\gamma} \\ \rho_1(\gamma)\mathrm{e}^{j\gamma} & 1 & \rho_1(\gamma)\mathrm{e}^{-j\gamma} \\ \rho_2(\gamma)\mathrm{e}^{j2\gamma} & \rho_1(\gamma)\mathrm{e}^{j\gamma} & 1 \end{pmatrix}. \tag{52}$$

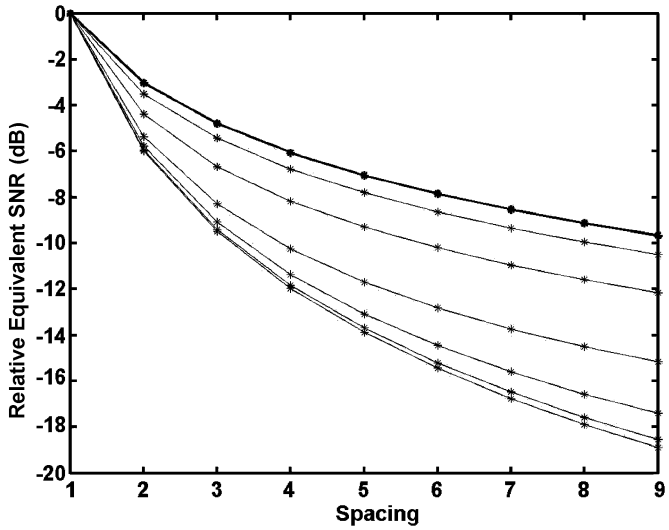

Fig. 21. Relative equivalent SNR as a function of spacing. The thick solid curve with stars marking integer spacing is for a 50-cycle square pulse. The thin solid curves with stars marking the integers are for 50-cycle pulses with q's of 0.1, 0.3, 1, 3, 10, and 30, top to bottom.

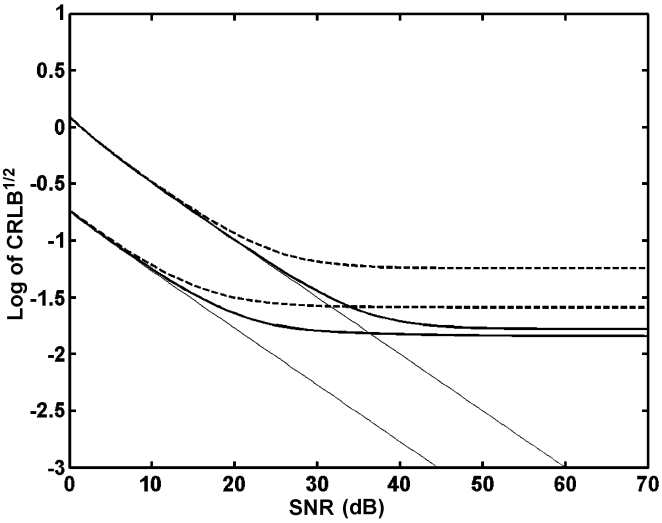

Fig. 22. $\mathrm{Log\,CRLB}^{1/2}$, where $\mathrm{CRLB}^{1/2}$ has the unit of radians, as a function of SNR for a six-element array (lower set of curves) and a two-element array (upper set of curves). The thin solid lines are the performance against uncorrelated noise only. The dashed lines are for both footprint shift and uncorrelated noise for a square pulse. The thick solid curves are for both footprint shift and uncorrelated noise for a pulse with a q of 3. The pulse length is 50 cycles and the electrical angle is 60°.

In practice, this situation represents the footprint shift process as being the only source of decorrelation from element to element. Of course, for this process, elements spaced further apart are less correlated (the correlation is represented by (28) for a square pulse and (24) for an exponential pulse). Now suppose an array with just two elements is considered but with different spacing as represented by the multiple-element array. For the two-element arrays, an SNR equivalent to ρ_k can be defined as

$$\mathrm{SNR}_k = \frac{\rho_k}{1-\rho_k} \tag{53}$$

where ρ_k is the correlation associated with the k^{th} spacing. Therefore, the equivalent SNR (SNR_k) for the various spacings can be compared to see if there is appreciable gain.

For example, consider a square pulse where the correlation from element to element is described by (28). If $N_p \gg (k\gamma/2\pi)$ where N_p is the number of carrier cycles in the pulse, then

$$\mathrm{SNR}_k = \frac{2\pi N_p}{k\gamma}. \tag{54}$$

This implies that

$$\mathrm{SNR}_k\ (\mathrm{dB}) = 10\log\frac{2\pi N_p}{\gamma} - 10\log k. \tag{55}$$

So the equivalent SNR drops by $10\log k$ dB from the value associated with the closest spacing.

As q is increased and as the pulse becomes less like a square pulse, the equivalent SNR drops even quicker, as shown in Fig. 21. In this figure, the relative equivalent SNR for increased spacings normalized to that for a spacing of one is plotted for various values of q. The electrical angle associated with a spacing of one is 60° for this plot. Since the equivalent SNR drops off so quickly for increased spacing, it is expected that the additional array elements will not significantly improve angle estimation performance against footprint shift noise over that obtained with a two-element array.

This lack of gain against footprint shift noise is illustrated in Fig. 22, where the $\mathrm{CRLB}^{1/2}$ is plotted for both six-element and two-element arrays with two pulse shapes (pulse length 50 cycles and an electrical angle of 60°). Three curves are shown for the two-element array and the six-element array. The reference curves for performance against uncorrelated noise are shown by thin solid lines and are parallel to each other with that of the six-element array being lower by a factor of 5.9 or 0.77 on the log scale as expected from the ratio in (51). The thick dashed curves are for performance against both footprint shift and uncorrelated noise for a square pulse. The plateau effect due to the footprint shift noise is evident as the SNR increases and the footprint shift effect dominates. Since the equivalent SNR for a square pulse does not fall off very quickly for increased spacings, there is some gain to be had for increasing the number of elements from 2 to 6.

The thick solid lines are for an exponential pulse with a q of 3. Although the exponential pulse yields a lower threshold than the square pulse, the difference in performance in terms of level of the plateau between the two-element and six-element array is not as large as for the square pulse. This reduced improvement is expected from the more rapid loss in an equivalent SNR for increased spacings as shown in Fig. 21.

The conclusion to be drawn from these results is that the effect of the footprint shift cannot be significantly mitigated by adding additional array elements. On the other hand, additional array elements do help combat uncorrelated noise (e.g., thermal noise), imperfections in practical arrays, and they facilitate the estimation of multiple angles. As was shown earlier, however, multiple snapshots help mitigate both the effects of footprint shift and uncorrelated noise.

V. General Discussion

From the results of Sections II–IV, it is evident that the CRLB is a useful tool for bounding the performance of angle estimation techniques for determining bottom location. Specifically,

performance for various scenarios can be estimated by plotting $2 \times \mathrm{CRLB}^{1/2}$ as a function of processing parameters such as the number of snapshots, the number of array elements, pulse length, and pulse rise time (as described by q). In this section, this tool is employed to predict the accuracy of bottom estimation employing angle estimation techniques.

The objective of angle estimation in the context of this paper is to determine the location of the bottom. To this point, the accuracy of angle estimation for extended targets such as the bottom is discussed from the point of view of determining the electrical angle. A shift is now made to the physical angle and ultimately bottom location accuracy.

There are many more combinations of parameters that could be discussed than are appropriate for a single paper. Therefore, this discussion focuses on the issue of multi-element arrays versus two-element arrays with the availability of multiple snapshots. Specifically, the performance of a two-element array with spacing $\lambda/2$ (where λ is the wavelength) is compared and contrasted with that of a six-element array with spacing $\lambda/2$ and a two-element array with spacing $5(\lambda/2)$, equivalent to the spacing of the two outside elements of the six-element array. It is shown that the performance of these arrays is essentially equivalent with respect to errors caused by footprint shift. However, the six-element array outperforms the other two with respect to uncorrelated noise.

The performance measure $2 \times \mathrm{CRLB}^{1/2}$ is used because it was shown to be representative of the angle estimation performance. Specifically, errors in the electrical angle are expected to be less than $2 \times \mathrm{CRLB}^{1/2}$ 81%–95% of the time depending on whether single snapshot statistics apply (i.e., post-estimation averaging of snapshots) or the statistics approach Gaussian (i.e., pre-estimation averaging of snapshots with no particular snapshot dominating). The CRLB for the physical angle θ is obtained from the CRLB of the electrical angle and (3) by [7, p. 929]

$$\begin{aligned}\mathrm{CRLB}(\theta) &= \left(\frac{\partial\gamma}{\partial\theta}\right)^{-2} \mathrm{CRLB}(\gamma) \\ &= \left(\frac{\lambda}{2\pi d\cos(\theta)}\right)^{2} \mathrm{CRLB}(\gamma). \end{aligned} \tag{56}$$

With this relationship, it is possible to make some general statements about the expected behavior of the CRLB for the physical angle with respect to footprint shift and uncorrelated noise.

A. Expected Performance Against Footprint Shift and Uncorrelated Noise

For a two-element array and a square pulse where the pulse length is long compared to the extent of the array, the $\mathrm{CRLB}(\gamma)$ is described by (42), and therefore,

$$\mathrm{CRLB}(\theta \,|\, \text{square pulse}) \simeq \left(\frac{\lambda}{2\pi d\cos(\theta)}\right)^{2} \frac{\gamma}{2\pi N_p}. \tag{57}$$

Substituting γ from (3)

$$\mathrm{CRLB}(\theta \,|\, \text{square pulse}) \simeq \frac{\lambda\sin(\theta)}{dN_p\left(2\pi\cos(\theta)\right)^{2}}. \tag{58}$$

Therefore, as the spacing d increases, it is expected that the CRLB for the physical angle will decrease. While this is true for a square pulse, it is not generally true for practical pulses.

In practical situations, the pulse is not square and the effective SNR falls off more rapidly as was shown in Fig. 21. Therefore, the dependence on spacing of the CRLB for the electrical angle is closer to d^2 rather than d as it is for the square pulse. Hence, it is found that the CRLB for the physical angle for practical situations will be relatively constant with respect to changes in spacing.

For uncorrelated noise, a specific expression for the CRLB for the electrical angle is available, namely (50). Therefore, the CRLB for the physical angle for the three arrays under consideration are expressed as follows:

1) two-element array with spacing d

$$\mathrm{CRLB}_1(\theta) = \left(\frac{\lambda}{2\pi d\cos(\theta)}\right)^{2} \frac{1}{\mathrm{SNR}_n} \tag{59}$$

2) M-element linear array with spacing d

$$\mathrm{CRLB}_2(\theta) = \left(\frac{\lambda}{2\pi d\cos(\theta)}\right)^{2} \frac{6}{M(M^2-1)\mathrm{SNR}_n} \tag{60}$$

3) two-element array with spacing $(M-1)d$

$$\mathrm{CRLB}_3(\theta) = \left(\frac{\lambda}{2\pi(M-1)d\cos(\theta)}\right)^{2} \frac{1}{\mathrm{SNR}_n}. \tag{61}$$

The ratio of CRLB_2 to CRLB_1 yields the reduction achieved over uncorrelated noise by a multi-element array and is

$$\frac{\mathrm{CRLB}_2(\theta)}{\mathrm{CRLB}_1(\theta)} = \frac{6}{M(M^2-1)} \tag{62}$$

which is the same as for the electrical angle [see (51)].

The ratio of CRLB_3 to CRLB_1 yields the reduction achieved over uncorrelated noise by spreading the two elements to a wider spacing. This reduction is

$$\frac{\mathrm{CRLB}_3(\theta)}{\mathrm{CRLB}_1(\theta)} = \frac{1}{(M-1)^2}. \tag{63}$$

Therefore, it is desirable to spread the two elements to achieve a lower CRLB for the physical angle. While this spread is desirable, it also presents problems in practice because multiple angle ambiguities that need to be sorted out are generated.

The relative goodness between a filled array and an array composed simply of two outside elements is expressed by the ratio

$$\frac{\mathrm{CRLB}_2(\theta)}{\mathrm{CRLB}_3(\theta)} = \frac{6(M-1)^2}{M(M^2-1)}. \tag{64}$$

This ratio is always less than or equal to 1 and for large M, the ratio approaches $6/M$, and therefore, the filled array generally outperforms the sparse array. For small M, however, the relative reductions are not that significant. For example, for $M = 3, 4, 5, \text{and } 6$, the reductions are 1, 0.9, 0.8, and 0.71, respectively. Therefore, for small arrays the large two-element array is

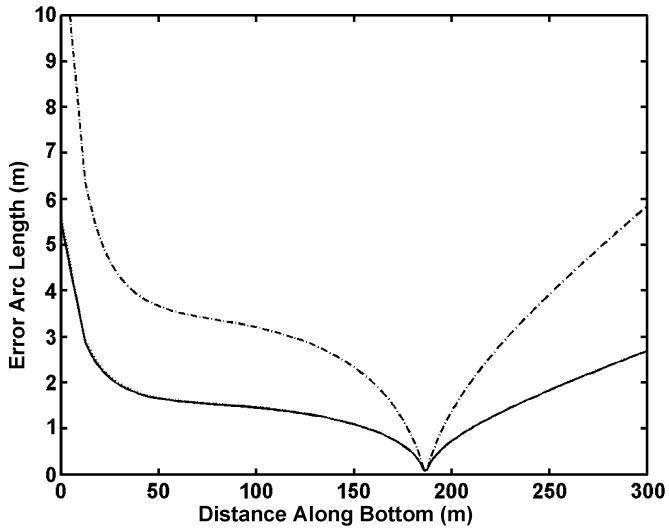

Fig. 23. Error arc length for $2 \times \mathrm{CRLB}^{1/2}$ as a function of distance along the bottom for three arrays, footprint shift only, and a square pulse. The dash–dot curve is for a two-element array with spacing $\lambda/2$. The solid curve is for a six-element array with element spacing $\lambda/2$. The dotted curve (hidden behind the solid curve) is for a two-element array with spacing $5\,(\lambda/2)$. The pulse length is 50 cycles, the frequency is 100 kHz, the depth is 50 m, the tilt angle is 15°, and the number of snapshots is 1.

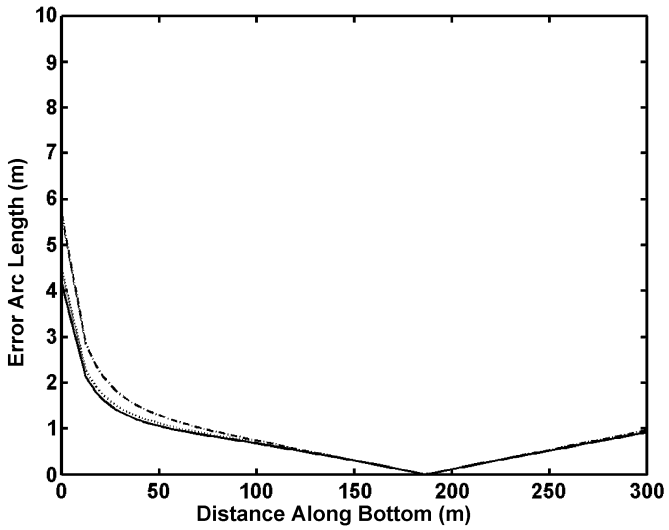

Fig. 24. Error arc length for the same scenario as Fig. 23 but the pulse has a q of 3.

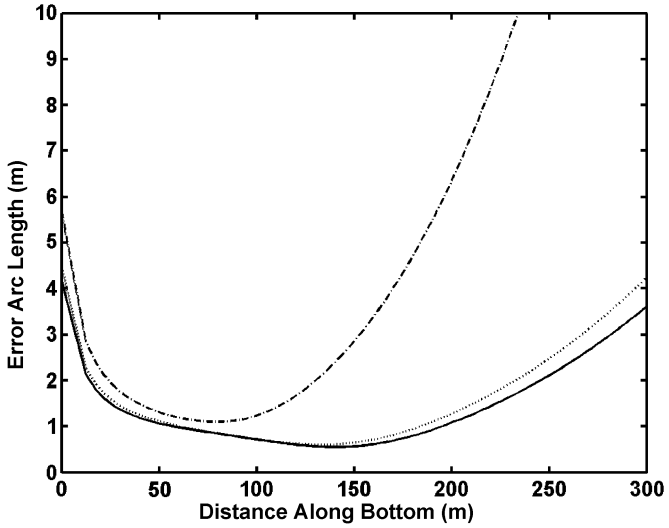

Fig. 25. Error arc length for the same scenario as Fig. 23 but the pulse has a q of 3, and uncorrelated noise is added with the same single-element SNR as shown in Fig. 11.

significantly better than the small two-element array, but marginally worse than the filled array with respect to performance against uncorrelated noise.

B. Bottom Estimation Accuracy

To compare the bottom estimation accuracy of the three arrays in a way that has significance in a practical context, the concept of an error arc length is employed. The actual error in space for angle estimation methods is along an arc centered at the true location, with a radius equal to the range as determined from the time of flight. The error arc length corresponding to $2 \times \mathrm{CRLB}^{1/2}$ is the product of the range and $2 \times \mathrm{CRLB}^{1/2}$ for the physical angle, namely

$$A = 2r\,\mathrm{CRLB}(\theta)^{\frac{1}{2}} \tag{65}$$

where A is the arc length, r is the range, and $\mathrm{CRLB}(\theta)$ is the Cramer–Rao bound for the physical angle.

The actual error in depth or distance along the bottom depends on the geometry. In other words, the estimated bottom falls within $\pm A$ along an arc centered at the true location with the same probability that the physical angle falls within $\pm 2\mathrm{CRLB}(\theta)^{1/2}$ or that the electrical angle falls within $\pm 2\mathrm{CRLB}(\gamma)^{1/2}$.

Employing the same physical scenario as that for Fig. 9 (a depth of 50 m, pulse length of 50 cycles, square pulse, a tilt angle of 15°, no uncorrelated noise, one snapshot) except that the smallest spacing is now $\lambda/2$ instead of 2λ, the results for arc length shown in Fig. 23 are obtained. The arc length for the two-element array with spacing $\lambda/2$ is shown by a dash–dot–dashed line, the arc length for the six-element array (spacing $\lambda/2$) by a solid line, and the arc length for the two-element array with spacing $5(\lambda/2)$ by a dotted line (cannot be seen due to overlap with the solid line). Note that the large spaced two-element array and the six-element array perform essentially the same. The small two-element array performs significantly worse.

If the pulse is changed from a square pulse to an exponential pulse with a q of 3, the performance shown in Fig. 24 is obtained. As expected, the overall performance is better and the short two-element array's performance more closely matches that of the other two, especially near broadside.

If uncorrelated noise is present and a q of 3 is maintained, the performance shown in Fig. 25 is obtained. For this figure, the noise was such that the SNR curve shown in Fig. 11 for a 50-cycle pulse is also valid. Note that the performance of the large two-element array is significantly better than that of the small two-element array at the further ranges where the uncorrelated noise dominates, but marginally worse than that for the six-element array. This behavior is expected from the results of the preliminary discussion.

The arc lengths shown in these figures do not characterize acceptable performance for a bottom estimation sonar, however,

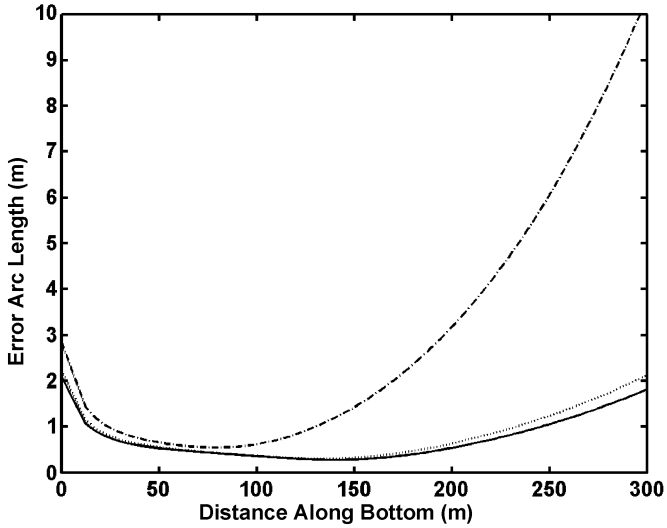

Fig. 26. Error arc length for the same scenario as Fig. 23 but the pulse has a q of 3, uncorrelated noise is added, and four snapshots are employed (pre-estimation averaging).

only one snapshot is used. If more snapshots are employed, better performance can be expected but at the loss of resolution. For example, if a 50-cycle pulse is employed at 100 kHz, the bottom resolution at far ranges is approximately $50\lambda/2 = 0.375$ m. If a resolution of 0.5% of range (i.e., 1.5 m) is desired, then uncorrelated snapshots can be used to reduce the estimation error. Fig. 26 shows the results for four snapshots. It is interesting that the results are essentially the same for a pulse length of 20 cycles and 10 snapshots, which maintains the same resolution on the bottom.

The frequency of operation can be increased to increase resolution along the bottom. This increase in frequency does not affect the error due to footprint shift because array sizes scale to the new frequency. The error due to uncorrelated noise, however, does change because the pulse length is reduced, reducing the number of scatterers in the pulse, hence, reducing the SNR. Therefore, if the noise level and the scattering strengths stay the same, the SNR drops by $10\log(f_H/f_L)$ dB, increasing the error due to uncorrelated noise by a factor $(f_H/f_L)^{1/2}$, where f_H and f_L are respectively the high and low carrier frequencies.

From an angle estimation point of view, there is little reason to prefer a filled array of say six elements to a sparse array of two elements of the same outside dimension. However, other considerations weigh heavily in favor of the filled array. First, if the sparse array is larger than $\lambda/2$, angle ambiguities have to be identified and corrected. Second, the sparse array can estimate only one arrival angle and, therefore, is not suitable for the large number applications where multiple signals arrive from different angles, whereas a filled array of M elements is capable of estimating $M-1$ arrival angles simultaneously. Third, it is desirable to average over a number of combinations of array elements to mitigate the effects of array imperfections such as crosstalk, and gain and phase variations present in real arrays.

The signals from a filled array can be processed in such a manner as to optimally combat the second and third issues listed above. For example, suppose for a shallow water survey, it is expected that there will possibly be a first surface bounce multipath and one water column target competing with the direct bottom backscatter signal. Then at least three degrees of freedom are required to estimate three angles, indicating the necessity of at least a four-element array. However, if a six-element array is employed, there are three combinations of four elements available by stepping along by one element. Employing these three combinations of four elements as separate arrays in a least squares technique to estimate angles supplies the number of degrees of freedom to estimate the expected number of arrivals. The three combinations also provide a degree of averaging over the array elements to mitigate array imperfections. These techniques are, for example, used in Benthos' C3D sonar to obtain a good estimate of the bottom in less than ideal conditions [10].

VI. Summary and Conclusion

In this paper, an analysis of high-resolution swath bathymetry was presented. The analysis included consideration of multiple-element arrays and multiple snapshots taken with these arrays. The primary analysis tool developed for comparing performance was the CRLB, which was applied to bound the variance on AOA estimation. This bound was developed for a common bottom model consisting of complex Gaussian scatterers. For this model, the CRLB was expressed in terms of the signal correlation matrix for the acoustic array. Two signal types were considered, a square pulse and an exponential pulse, for which the correlation matrices are presented; hence, the CRLB was determined. Through this analysis, two error mechanisms were identified as being important for the short-pulse (high-resolution) swath bathymetry sonar application: decorrelation across the array caused by independent noise from element to element such as thermal noise; and decorrelation across the array caused by footprint shift.

To validate the CRLB as a useful tool for analyzing AOA accuracy, the problem of estimating bottom position with a two-element array was treated in detail using the bound, probability analysis, and simulation. It was shown that the true variance of angle estimation is difficult to obtain through simulation and, hence, supporting analysis is required. As a result of the probability analysis, a criterion for evaluating angle estimation performance based on the CRLB was chosen, namely errors in estimating the AOA are expected to be less than $2 \times \mathrm{CRLB}^{1/2}$ 81–95% of the time, depending on whether one or more snapshots are used for the estimate.

Multiple snapshots of the signals across the two-element array were employed to decrease the error in estimating the AOA. Two methods for combining the snapshots were discussed, pre-estimation averaging and post-estimation averaging. It was shown that pre-estimation averaging outperformed post-estimation averaging in the sense that for the former, the variance of the estimation approached the CRLB, while for the latter, the variance remained at twice the CRLB for 100 trials. Nevertheless, it was also observed that the post-estimation averaging may be a more robust technique in certain situations if the underlying statistical model intensities change for different snapshots.

The usefulness of employing multiple array elements to increase AOA estimation performance was also investigated. It was shown that in terms of angle estimation performance, the detrimental effect of footprint shift cannot be significantly mitigated by additional array elements. However, additional elements do help in mitigating the effect of uncorrelated noise (e.g., thermal noise).

In comparing multiple-element performance to that of two-element arrays, an M-element linear array was compared with 2 two-element arrays, one with $\lambda/2$ spacing and the other with $(M-1)\lambda/2$ spacing (i.e., the same dimensions as the outer elements of the multi-element array). Expressions for performance against footprint shift and uncorrelated noise were obtained.

Finally, bottom estimation accuracy was compared for a six-element array and 2 two-element arrays. For this comparison, a new measure of performance was defined called "the error arc length" based on the angle error determined from the CRLB. The error arc length gives a spatial, or length dimension to the error that facilitates contextual interpretation. Using this measure, it was found that the six-element array performed only slightly better against uncorrelated noise than the two-element array with $5\lambda/2$ spacing, whereas they performed equally against footprint shift. Therefore, in consideration of only these two effects, there is little reason to use a multi-element array. However, in practical scenarios, where two or more signals may be incident on the array at the same time (e.g., multipath environments), a filled array offers additional degrees of freedom that permit the estimation of multiple angles. In addition, a filled array does not suffer from angle ambiguity problems associated with a widely spaced two-element array. Furthermore, certain imperfections encountered in practical transducer arrays can be mitigated by the spatial averaging available with a filled array. Therefore, it is concluded that filled arrays are preferred over two-element arrays for practical reasons.

Appendix I
Expression for δx

From Fig. 27

$$r_1 = \sqrt{h^2 + x^2} \tag{I.1}$$

and

$$r_2 = \sqrt{(h + d\cos(\theta_t))^2 + (x - d\sin(\theta_t))^2}. \tag{I.2}$$

Since the signal samples are taken at the two elements at the same time, the time of flight for the two path is equal, hence,

$$2r = r_1 + r_2. \tag{I.3}$$

The expression for δx is

$$\delta x = h\left(\tan(A) - \tan(\phi_0)\right). \tag{I.4}$$

But

$$\tan(A) = \frac{2(x + \delta x)}{2h} \tag{I.5}$$

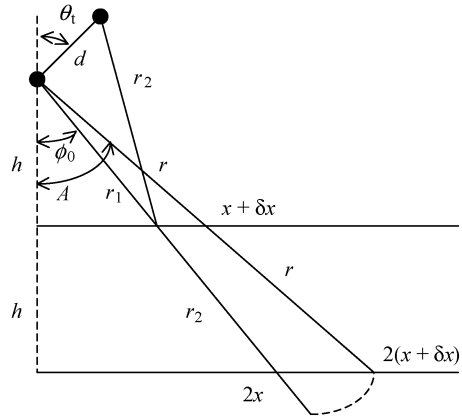

Fig. 27. Geometry for calculation of δx.

and using (I.3)

$$(2(x + \delta x))^2 = (2r)^2 - (2h)^2 = (r_1 + r_2)^2 - (2h)^2 \tag{I.6}$$

hence,

$$\tan(A) = \frac{\sqrt{(r_1 + r_2)^2 - (2h)^2}}{2h}. \tag{I.7}$$

Substituting (I.7) into (I.4) results in

$$\delta x = h\left(\frac{\sqrt{(r_1 + r_2)^2 - (2h)^2}}{2h} - \frac{x}{h}\right). \tag{I.8}$$

Using (I.1) and (I.2) and collecting and rearranging terms results in

$$\delta x = \left(\frac{r_1^2}{4}\left(2 + \frac{d^2}{r_1^2} + \frac{2d}{r_1}\cos(\phi_0 + \theta_t) + 2\sqrt{1 + \frac{d^2}{r_1^2} + \frac{2d}{r_1}\cos(\phi_0 + \theta_t)}\right) - h^2\right)^{\frac{1}{2}} - x. \tag{I.9}$$

Equation (I.9) is the exact expression for δx. Approximations are now made consistent with the bottom estimation problem. Neglecting all d^2/r_1^2 terms since $d \ll r_1$ and noting also that

$$\frac{2d}{r_1}\cos(\phi_0 + \theta_t) \ll 1 \tag{I.10}$$

so that

$$2\sqrt{1 + \frac{2d}{r_1}\cos(\phi_0 + \theta_t)} \simeq 2 + \frac{2d}{r_1}\cos(\phi_0 + \theta_t). \tag{I.11}$$

Then

$$\delta x \simeq \sqrt{r_1^2 - h^2 + dr_1\cos(\phi_0 + \theta_t)} - x. \tag{I.12}$$

But as $r_1^2 - h^2 = x^2$

$$\delta x = x\sqrt{1 + \frac{dr_1}{x^2}\cos(\phi_0 + \theta_t)} - x. \tag{I.13}$$

If

$$\frac{dr_1}{x^2}\cos(\phi_0 + \theta_t) \ll 1 \tag{I.14}$$

in other words, not near nadir, then

$$\delta x \simeq x\left(1+\frac{dr_1}{2x^2}\cos(\phi_0+\theta_t)\right)-x \tag{I.15}$$

and

$$\delta x \simeq \frac{dr_1}{2x}\cos(\phi_0+\theta_t). \tag{I.16}$$

Now $x/r_1 = \sin(\phi_0)$, so

$$\delta x \simeq \frac{d}{2}\frac{\cos(\phi_0+\theta_t)}{\sin(\phi_0)} \tag{I.17}$$

which is the desired result.

Appendix II
Variance for Preestimation Averaging

As was shown in Section III-A, the correlation of the signals for a two-element array can be modeled using an effective SNR. Therefore, the signals can be considered composed of signal plus an uncorrelated noise term as shown in the following:

$$s_1 = a\exp(j\phi)+n_1 \tag{II.1}$$
$$s_2 = a\exp(j\phi+j\gamma)+n_2 \tag{II.2}$$

where s_1 and s_2 are the signals at array elements 1 and 2, respectively, a is a Rayleigh random variable representing the amplitude, ϕ is a random variable distributed uniformly over $\pm\pi$, and n_1 and n_2 are the effective uncorrelated noises.

For pre-estimation averaging, the test statistic $s_1^* s_2$ is summed over N snapshots and then the angle is determined as follows:

$$S = \sum_{k=1}^{N} s_{1k}^* s_{2k} \tag{II.3}$$

and

$$\hat{\gamma} = \arctan\left(\frac{\mathrm{Im}(S)}{\mathrm{Re}(S)}\right) \tag{II.4}$$

where $\hat{\gamma}$ is the estimated electrical angle, $\mathrm{Im}(\cdot)$ is the imaginary part, $\mathrm{Re}(\cdot)$ is the real part, and it is assumed that the arctan function takes quadrants into account. Noting that

$$s_1^* s_2 = a^2\exp(j\gamma)+an_2\exp(-j\phi) + an_1^*\exp(j\phi+j\gamma)+n_1^* n_2 \tag{II.5}$$

the following is obtained for S

$$S = \exp(j\gamma)\sum_{k=1}^{N} a_k^2 + \sum_{k=1}^{N} a_k n_{2k}\exp(-j\phi_k) + \exp(j\gamma)\sum_{k=1}^{N} a_k n_{1k}^*\exp(j\phi_k)+\sum_{k=1}^{N} n_{1k}^* n_{2k}. \tag{II.6}$$

Assuming the SNR is large the last term is neglected.

If, for the present, the a_k's are assumed to be known constants, the two remaining sums that include noise terms are Gaussian circular symmetric random variables with component variances $\sigma_n^2\sum_{k=1}^{N} a_k^2$. Since these sums are composed of independent noise terms, the sum of the two sums is also a Gaussian circular symmetric random variable with twice the component variance, namely

$$\sigma^2 = 2\sigma_n^2\sum_{k=1}^{N} a_k^2. \tag{II.7}$$

Again, remembering that for the present, the a_k's are assumed to be known constants, Fig. 28 characterizes the situation, where

$$r_s = \sum_{k=1}^{N} a_k^2. \tag{II.8}$$

Therefore,

$$\mathrm{var}(\hat{\gamma}\,|\,r_s) \simeq \frac{\sigma_z^2}{r_s^2} = \frac{\sigma^2}{r_s^2} = \frac{2\sigma_n^2 r_s}{r_s^2} = \frac{2\sigma_n^2}{r_s} \tag{II.9}$$

and the unconditional variance can be determined by

$$\mathrm{var}(\hat{\gamma}) = \int_0^\infty \mathrm{var}(\hat{\gamma}\,|\,r_s)\,f(r_s)dr_s \tag{II.10}$$

where $f(r_s)$ is the probability density of r_s. Since r_s is the sum of independent squared Rayleigh random variables, it is the sum of independent exponential random variables. Therefore,

$$f(r_s) = \frac{r_s^{N-1}}{(2\sigma_s^2)^N\,\Gamma(N)}\exp\left(-\frac{r_s}{2\sigma_s^2}\right) \tag{II.11}$$

where σ_s^2 is the parameter describing the original Rayleigh density of the a_k's.

Therefore, the unconditional variance obtained using (II.9)–(II.11) is

$$\mathrm{var}(\hat{\gamma}) \simeq \int_0^\infty \frac{2\sigma_n^2}{r_s}\frac{r_s^{N-1}}{(2\sigma_s^2)^N\,\Gamma(N)}\exp\left(-\frac{r_s}{2\sigma_s^2}\right)dr_s. \tag{II.12}$$

Solving (II.12) results in

$$\mathrm{var}(\hat{\gamma}) = \frac{2\sigma_n^2}{(N-1)2\sigma_s^2} = \frac{1}{(N-1)\mathrm{SNR}_e} \tag{II.13}$$

where SNR_e is the effective SNR defined as σ_s^2/σ_n^2.

Since

$$\mathrm{CRLB}(\hat{\gamma}) = \frac{1}{N\mathrm{SNR}_e} \tag{II.14}$$

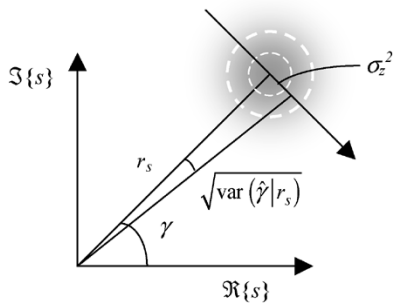

Fig. 28. Illustration of probability density for given r_s.

the desired result is obtained, namely

$$\frac{\mathrm{var}(\hat{\gamma})}{\mathrm{CRLB}(\hat{\gamma})} \simeq \frac{N}{N-1}. \tag{II.15}$$

The approximate sign is used to indicate that the expression is valid only for high signal-to-noise ratios.

REFERENCES

[1] P. N. Denbigh, "Swath bathymetry: Principles of operation and an analysis of errors," *IEEE J. Ocean. Eng.*, vol. 14, no. 4, pp. 289–298, Oct. 1989.

[2] C. de Moustier, "State of the art in swath bathymetric survey systems," *Int. Hydrogr. Rev.*, vol. 65, no. 2, pp. 25–54, 1988.

[3] P. H. Kraeutner and J. S. Bird, "Principle components array processing for swath acoustic mapping," in *Proc. Oceans'97*, Halifax, Nova Scotia, pp. 1246–1254.

[4] ——, "Beyond interferometry, resolving multiple angles-of-arrival in swath bathymetric imaging," in *Proc. Oceans'99*, Seattle, WA, pp. 37–45.

[5] X. Lurton, "Swath bathymetry using phase difference: Theoretical analysis of acoustic measurement precision," *IEEE J. Ocean. Eng.*, vol. 25, no. 3, pp. 351–363, Jul. 2000.

[6] G. Jin and D. Tang, "Uncertainties of differential phase estimation associated with interferometric sonars," *IEEE J. Ocean. Eng.*, vol. 21, no. 1, pp. 53–63, Jan. 1996.

[7] H. L. Van Trees, *Optimum Array Processing: Part IV of Detection, Estimation, and Modulation Theory*. New York: Wiley-Interscience, 2002.

[8] D. Middleton, *Introduction to Statistical Communication Theory*. New York: McGraw-Hill, 1960.

[9] J. S. Bird, S. Asadov, and P. Kraeutner, "Improving arrays for multi-angle swath bathymetry," in *Proc. Oceans'2003*, San Diego, CA, pp. 2085–2092.

[10] Benthos, Inc.. (2003, Dec.) C3D Sonar Imaging System. [Online]www.benthos.com

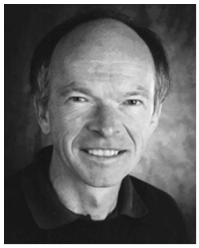

John S. Bird received the B.S. degree in electrical engineering in 1973 from the University of British Columbia, Vancouver, BC, Canada, and the Ph.D. degree in electrical engineering from Carleton University, Ottawa, ON, Canada, in 1980.

He worked for the Defence Research Establishment Pacific, Victoria, BC, from 1973 to 1981, where he was engaged in signal processing and detection studies related to passive sonar. From 1981 to 1987, he continued these studies but in the context of land- and space-based surveillance radars while on loan to the Communications Research Centre from the Defence Research Establishment Ottawa. During this time, he also worked in the area of satellite spread spectrum communications. He is currently with the School of Engineering Science at Simon Fraser University in Burnaby, BC, where his research interests include signal processing, underwater acoustics, sonar, bottom mapping, autonomous underwater vehicles, limnology, and lake exploration.

Geoff K. Mullins received the B.A.Sc. degree in engineering physics in 2001 from Queen's University, Kingston, ON, Canada, and the M.A.Sc. degree in engineering physics from the University of British Columbia, Vancouver, BC, Canada, in 2003. He has been working towards the Ph.D. degree at Simon Fraser University, Vancouver, BC, Canada, since 2003.

From 2001 to 2003, he worked on High Temperature Superconductivity at the University of British Columbia. At the School of Engineering Science at Simon Fraser University, he switched fields to underwater acoustics where he is working on bottom classification using MASB sonar.